UNIVERSITEIT VAN AMSTERDAM

VU VRIJE UNIVERSITEIT AMSTERDAM

MSc Chemistry
Molecular sciences

Master Thesis

Formation of complex perovskite heterostructures:

A step towards understanding the interfaces of perovskite solar cells

---

by

Floris Blom
11296062

42 EC
July 2021-February 2022

Supervisor
Prof. Dr. Bruno Ehrler
Dr. Esther Alarcon Llado
Examiner:
Prof. Dr. Erik Garnett

Second Examiner:
Prof. Dr. Joost Reek

AMOLF physics of functional complex matter

AMOLF, Amsterdam, the Netherlands, July 19th 2022

Abstract

Photovoltaic devices are going to play a big role in mitigating fossil fuel usage. Organic metal halide perovskites will contribute in expanding the usage of these photovoltaic devices, however a lot of phenomena in perovskite solar cells are still not clearly understood, such as recombination at perovskite solar cell (PSC) interfaces. In this research, a step towards looking at these interfaces is made by creating a 2D/3D heterojunction perovskite device and finding out what the effect of this 2D/3D heterojunction is on the charge carrier dynamics compared to an analogous 3D perovskite. These devices will be made on a patterned interdigitated back-contact (IBC) structure in order to study spatially resolved photoluminescence of the device. An interlayer of 2D perovskite is selectively synthesised on top of IBC contacts with a nickel oxide hole transport layer in a two-step process. First, selective electrodeposition is used to form lead dioxide on nickel oxide. Secondly, the lead dioxide is converted to $(PEA)_2PbI_4$ by chemical vapour deposition. On top of this 2D perovskite layer, deposition of a 3D perovskite layer has been attempted, through different deposition methods such as spin coating, stamping and thermal evaporation of which thermal evaporation produced the desired 2D/3D heterojunction. By SEM imaging, XRD and PL mapping, it was concluded that a 2D/3D heterostructure can be formed. However, during the formation of this heterojunction a higher dimensional n=2 perovskite layer is formed as well. TRPL measurements show that the charge carrier lifetimes of the heterojunction are increased compared to the 3D perovskite analogue.

Table of Contents

Abstract 2

1. Introduction 4

2. Theoretical background 9

2.1 Perovskite structures 9

2.2 Local deposition of NiO_x/Au contacts 10

2.3 Electrochemistry 11

2.4 Chemical Vapour Deposition. 15

2.5 3D perovskite deposition 16

3. Results & Discussion 17

3.1: Electrodepostion of PbO_2 on NiO_x/ITO films 17

3.2 PbO_2 conversion to $(PEA)_2PbI_4$ by Chemical Vapour Deposition 20

3.3 Electrodeposition and CVD on patterned NiO_x/Au contacts. 24

3.4 2D/3D fabrication 28

3.5 Thermal evaporation: 31

3.6 Transient PL on 2D/3D heterojunctions 37

4. Conclusion and Future Outlook 40

5. Acknowledgements 41

6. Experimental 42

Sample fabrication 42

Characterization: 43

7. References: 45

1. Introduction

The most recent scientific report on climate change has unequivocally shown that human influence has warmed the atmosphere, ocean and land.[1] Most of this warming originates from greenhouse gas emission, primarily from combustion of fossil fuels for energy use. Until 2050, the global energy use is expected to increase compared to 2020, which mostly results from economic growth and population growth in developing countries (Figure 1a).[2] In order to prevent the rise in emission of greenhouse gasses associated with this increase in energy consumption it is of the utmost importance that more sources of sustainable energy are researched and implemented in the coming decades. One of the most important sustainable energy sources that can be used is the sun. Photovoltaic devices can harness the power of the sun and these devices have seen a significant rise in commercial usage over the past years.[1] Since solar power will be a big part of the energy mix of the future (Figure 1b), research in improving photovoltaic materials has high priority in both academic and industrial setting.

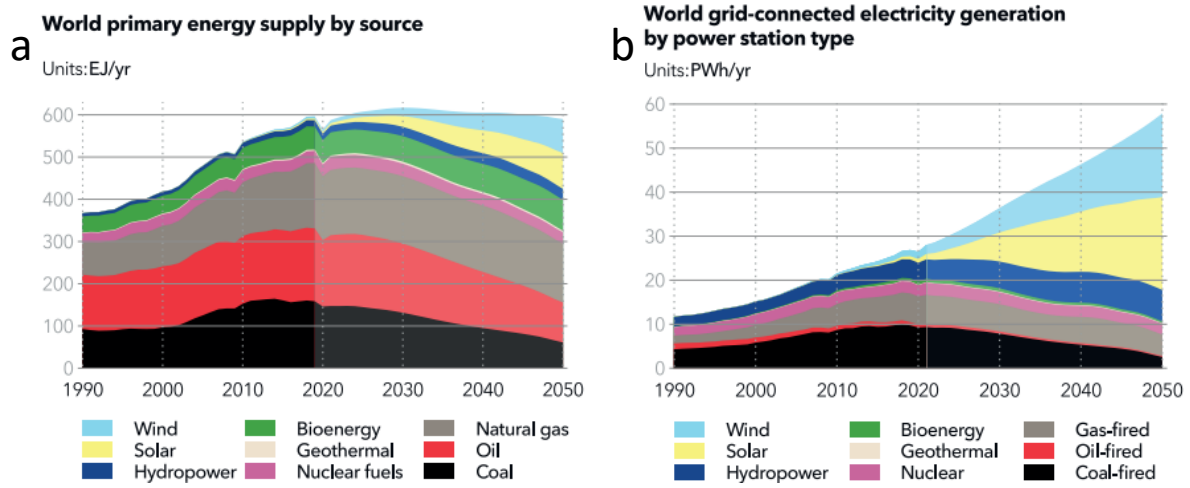

Figure 1: (a) World primary energy supply by source and (b) world electricity generation by power station type. Figure from: DNV AS 2021.[2]

Metal halide perovskites are one of the promising classes of photovoltaic materials that have recently attracted significant amount of attention for application in optoelectronic devices.[3] Similar to other photoactive semiconductors, in perovskites the charge carriers (electrons and holes) are generated by light absorption which is subsequently converted into electrical energy by extraction of those charge carriers. In particular, these materials are excellent light absorbers because of their high dielectric constant, direct band gap, high carrier mobility, long carrier lifetime, and facile processing at low temperature.[4–6] Recently, a power conversion efficiency (PCE) of 25.5% was achieved for a single-junction perovskite solar cell, which is close to the feasible theoretical limit for single-junction solar cells (33.7%).[7] These perovskites were originally made up of a composition of ABX_3, consisting of A = small cationic species (e.g. methylammonium, formamidinium, or cesium), B = divalent metal (e.g. lead or tin), and X = halide (e.g. iodide, bromide, or chloride). The metal and halide components form an octahedral structure, while A-site cations are occupying the interstitial space between these octahedrons (Figure 2). By material engineering more complicated structures with multiple cationic species or halides can be synthesised.

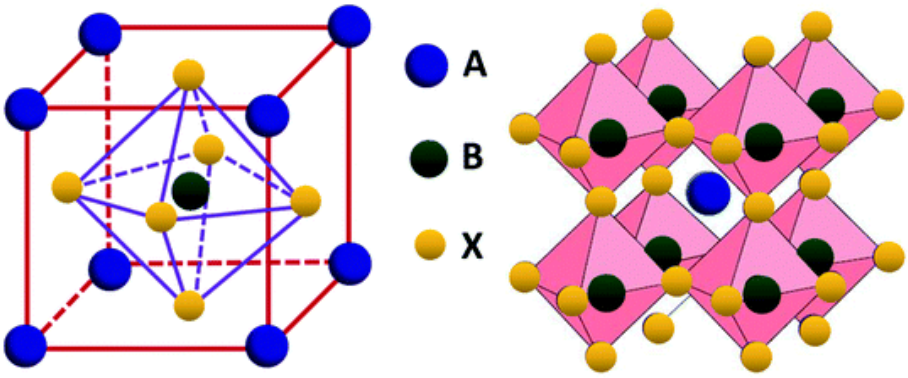

***Figure 2**: Structure of perovskites with ABX3 composition. Figure from: Wang et al., 2019.8*

When perovskites are used in a photovoltaic device, a so called perovskite solar cell (PSC), it usually consists of multiple, stacked layers: electrodes, a hole transport layer (HTL) and electron transport layer (ETL) and the perovskite absorber layer, which is usually sandwiched between the two charge transport layers. This results in either a conventional (n-i-p) or inverted (p-i-n) device structure. A schematic overview is shown below in Figure 3. Through the energy level alignment of the charge transport layers with the other layers charges (either holes or electrons) are extracted selectively. Depending on the type of semiconductor the holes (p-type) or the electrons (n-type) can be the majority carriers of the current. The majority carriers can be extracted to the electrode through the transport layer without major losses by providing a high corresponding electric conductivity.[9] Minority carriers can be blocked by a high bandgap which acts as an energetic barrier. At the other transport layer this effect is exactly the other way around.

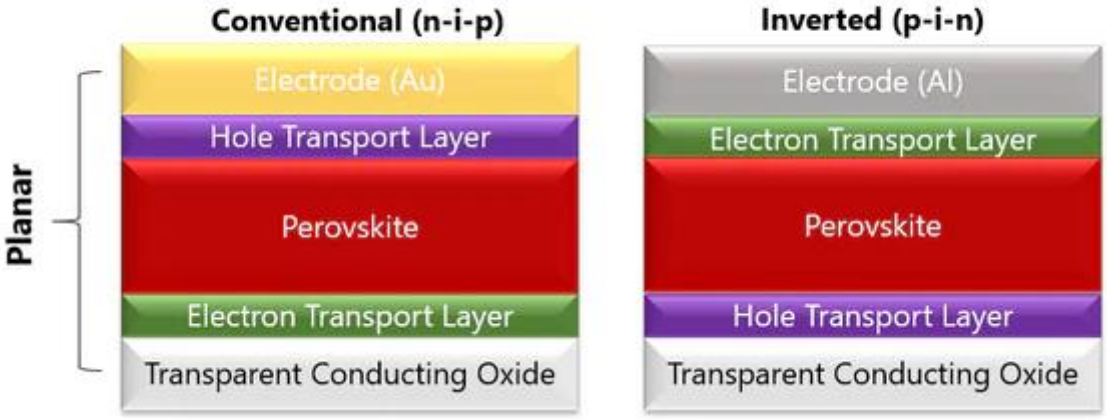

***Figure 3**: General composition of multi-layered planar PSC devices. Figure from: Ossila, 2021.[10] In these devices the transparent conducting oxide layers are working as electrodes, just like Au and Al.*

When the transport layer is not aligned well enough with the perovskite absorber this can lead to a barrier to majority carrier transport across the interface region, leading to low effective conductivity. It could also lead to current flow of minority carriers to the interface/into the transport layer, which could lead to non-radiative recombination between minority and majority carriers. In turn these losses lead to a lower open-circuit voltage (V_{oc}) and fill-factor (FF). Therefore suppressing these losses between the perovskite and the charge transport layers is important to maximise the V_{oc} and FF of PSC devices.[11]

Despite their beneficial properties, perovskites/PSCs have several fabrication challenges that need to be addressed before upscaling and commercialization can take place. These challenges include poor morphology control, energy level alignment mismatches, and the presence of bulk and interfacial defects. The interfacial defects are the main contributors to non-radiative charge recombination in the PSC.[12–14] Non-radiative recombination in full-stack PSCs mostly takes place at one or both of the perovskite/transport layer heterojunctions.[9,15] In addition, the interfacial recombination can occur across the interfaces between charges in the transport layer and minority carriers in the perovskite, or within the transport layer itself.[16–18]

Studies on surface engineering to decrease the interfacial recombination have led to the use of additives and additional (atomic) layers, which are employed in two different ways: reducing the number of defect states via chemical passivation or reducing the interfacial transfer rate through an energetic barrier for minority carriers (e.g. wide-gap interlayers). Most research has focused on the former to improve PCE.[9] However with the latter, a thin insulating layer can be used as a tunnelling layer to avoid direct contact between the majority carriers in the transport layer from the minority carriers in the bulk perovskite.[18–20] A way to create a wide-gap interlayer is the application of two-dimensional (2D) perovskite layers. The two-dimensionality is referring to the layering of the corner sharing inorganic octahedra.[21] These layers of inorganic material are separated by bulky organic molecules that replace the small cationic species at the A site (Figure 2). The bulky organic molecules are bound to the inorganic octahedra through hydrogen bonds, which causes the hydrophobic chain to be directed away from the inorganic perovskite layers. In this way organic bilayers are formed that separate neighbouring sheets of perovskite octahedra, which creates a repeating pattern.[22] The dimensionality, *n*, indicates the amount of inorganic sheets in between each organic bilayer. In this way pure 2D perovskites are denoted as $n = 1$. At $n \geq 2$ the small A-site cations are also included in the perovskite formula which means a quasi-2D structure is formed where a higher number of layers of inorganic octahedrons can reside between the organic bilayer (Figure 4).[23] At $n = \infty$ 3D perovskite is formed. 2D perovskites are different from their 3D counterparts by their high stability towards moisture and low ion migration.[24] Additionally, 2D perovskites exhibit excellent structural diversity, and their properties can be tuned by the layer thickness and the spacer cation.[22] However, simultaneously the 2D perovskite hinders charge carrier separation and extraction due to the presence

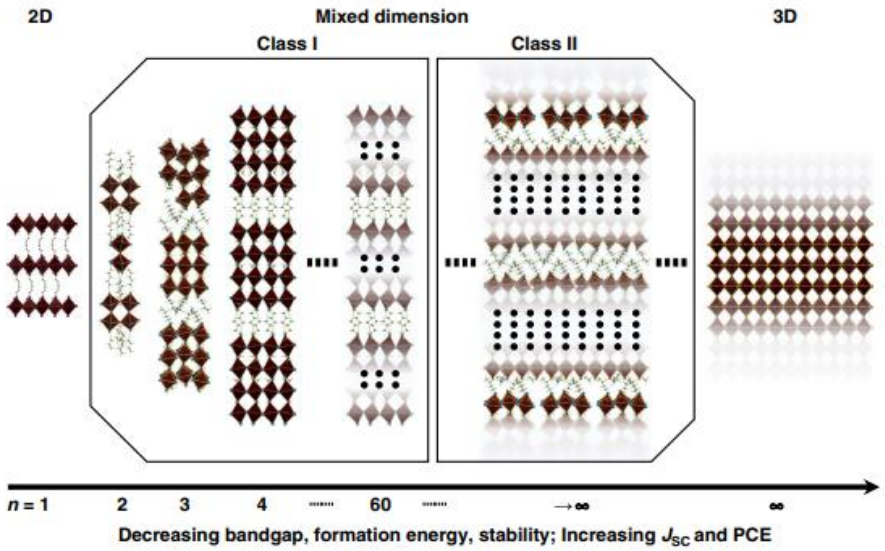

***Figure 4**: Dimensionality engineering. Effects of perovskite phase evolution on chemical and physical properties. Figure from: Nazeeruddin et al., 2019.[23]*

of these layers of larger organic molecules which leads to higher exciton binding energies. It would be expected that a long chain cation would lack the ability to transfer charges efficiently through the layers of the spacer molecules due to the difference in dielectric constant with the inorganic layer.[25] Therefore, 2D perovskites can be seen as naturally formed quantum wells, where the organic spacers act as the barriers and the inorganic layers as the wells.[26] This leads to higher bandgaps (~2.36 eV) and therefore a lower emission wavelength of roughly 520 nm.

By inserting a very thin interlayer of this 2D perovskite material between the 3D perovskite and a charge transport layer the beneficial properties of both types of perovskite can be combined while simultaneously diminishing the cons of the 2D perovskite.[27] Progress has been made with the 2D/3D perovskite heterostructure based on different spacer cations to reduce the interfacial recombination and subsequently the efficiency and stability of the solar cells.[28] Nonetheless, detailed understanding of the mechanism by which 2D perovskite limits interfacial recombination and increases stability of perovskite solar cells still has to be developed.

Usually the 2D/3D interface is created by mixing 2D precursor with 3D precursor solutions which are then spin-coated together.[29–31] Other solution based processes include dip coating of the 3D perovskite in a solution of an 2D precursor solution and spin-coating of a 2D precursor solution on top of an existing 3D perovskite layer.[32–34] Even though these solution-based processes form a 2D/3D structure they have the drawback that unintentionally quasi-2D phases or different (non-crystalline) phases are formed, therefore a mixed material is formed rather than a clear interface that has a clear-cut distinction between phases. This results in poor transport of charge carriers and makes it more difficult to investigate the interfaces between the two dimensions.[35] Two different solvent free pathways to create a clean 2D/3D heterojunction have been investigated recently to deal with this problem: multi-source thermal evaporation of a 2D/3D heterojunction[36–38] and solid-phase in-plane growth.[39] When this 2D/3D interface is investigated this commonly is done in either a stacked PSC or in incomplete devices. Furthermore, these methods have been employed to make 2D perovskite on top of 3D and not so much 3D perovskite on top of 2D perovskite. In order to study the interfaces between the different PSC layers, interdigitated back contacts (IBC) can be employed.

In an IBC device the electrodes are located on the backside of the solar cell in an interdigitated fashion, meaning that the hole and electron selective electrodes are alternating and interlocking in a comb like structure.[40] In this way the perovskite layer is the top layer of the device, which is helpful to prevent surface damage in further manufacturing steps. Due to the structural design of the IBC properties of a heterojunction can be studied spatially and characterised *in-operando*.[40] Another advantage of the IBC-devices is the flexibility in processing and passivation treatments.[41] However, to create an interlayer between the transport layers and the 3D perovskite in an IBC the 2D perovskite has to be created underneath the 3D perovskite. This is something that has not been studied often, even in conventional sandwich structures.[42] Methods such as spin-coating usually don't work here because it would lead to mixed perovskite phases.

Besides conventional methods of perovskite film formation, such as the aforementioned spin-coating, there have been developments in film formation such as thermal evaporation and electrodeposition. Typically in an electrodeposition process solid metals are deposited on a surface by electrochemical reduction of a desired metal precursor (e.g. dissolved metal salts).[43] The process is performed by direct transfer of electrons from a working electrode, on which a potential can be applied to influence the rate of electron generation, as well as crystallite nucleation and growth. Electrodeposition is a versatile technique for the production of surface coatings, due to the operation at ambient temperature, rapid deposition rate, and relatively low cost.[44] Furthermore the thickness can be controlled by adjustment of the deposition time and the current density.[45] This method can be used for deposition of perovskite

on a wide range of complex shape substrates as long as they are conductive.[46,47] This enables deposition of perovskite with high spatial controllability. The electrodeposition method is used to deposit the lead precursor films (e.g. Pb^0, PbO, PbO_2) which in turn can be chemically converted into the perovskite by different two-step conversion processes.[45,47–49] The electrochemical deposition and vapor conversion method of Lee et al. will be adapted in this research to selectively create a 2D perovskite layer on top of IBC contacts with a HTL. On top of the 2D perovskite layer a 3D perovskite layer will be deposited, which will be compared to a regular 3D perovskite layer. Therefore this research has two different aims. First it will be investigated if this 2D/3D heterostructure can be formed and characterised on an IBC patterned substrate. Second, it will be investigated what influence this interlayer has on the charge carrier dynamics of the 3D perovskite.

2. Theoretical background

This chapter discusses the theoretical background for the techniques and the methodology used to create the 2D/3D perovskite heterojunctions. The process consists of four consecutive steps to create a patterned 2D perovskite underneath a 3D perovskite layer. Before discussing these steps a short overview of the used perovskite materials will be given. After that the local deposition area is discussed. Which is followed by the concepts of electrochemistry and PbO_2 deposition, based on previous research in the field[44,45,47,50], including a description of the electrochemical cell used in this work. Subsequently the conversion of PbO_2 to perovskite with chemical vapour deposition will be explained. Finally, the various methods of deposition of a 3D layer on top of the 2D layer will be touched upon.

2.1 Perovskite structures

The 2D perovskite that will be used in this research is phenylethylammonium lead iodide ($(PEA)_2PbI_4$) (Figure 5). PEA^+ is an aromatic cation that facilitates formation of layered 2D perovskite due to the phenyl moiety size and ring rigidity.[26] The incorporation of the aromatic ring is believed to be beneficial for charge transport compared to the commonly used 2D perovskite cation butylammonium (BA^+). These aromatic rings are parallel to each other because of π−π stacking, while between the sheets, the rings adopt a face-to-edge configuration. Due to the mono-ammonium moiety a Ruddlesden-Popper configuration, which offsets the stacking of the inorganic slabs in the a and b directions.[51] This perovskite has a bandgap of ~2.3 eV and a PL emission wavelength of 525 nm.[52] This large bandgap , compared to the bandgap of 3D perovskites, might be one of the reasons why it is so effective in reducing non-radiative recombination at the interface of the 3D perovskite.

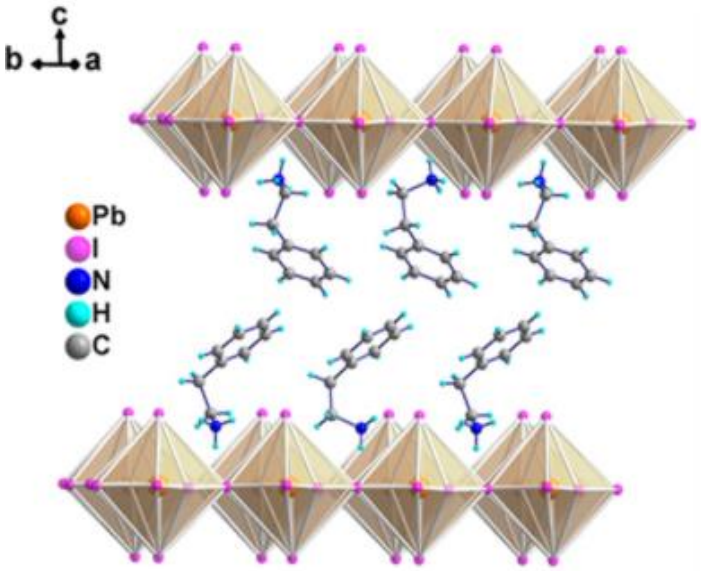

***Figure 5**: Crystal structure of $(PEA)_2PbI_4$. Figure from: Kanatzidis et al., 2021[26]*

The 3D perovskite used in this research is a double cation (cesium, formamidinium), double halide (iodide, bromide) lead perovskite ($FA_{0.7}Cs_{0.3}Pb(I_{0.9}Br_{0.1})_3$), which has shown improved stability over conventional $MAPbI_3$ and a bandgap of ~1.74 eV.[53] This compound has shown to be stable towards photoinduced halide segregation. Furthermore it is possible to synthesize this perovskite with different techniques (e.g. solution processing and evaporation techniques).

An important factor to be able to indicate formation of a 2D/3D heterojunction is the ability to see different properties of both perovskites simultaneously. The difference in emission wavelength and

energy levels were the main reason to select the aforementioned 2D and 3D perovskites. The differences in energy levels lead to a straddling gap and due to the differences in bandgap PL studies can be used to characterize both perovskites.

2.2 Local deposition of NiO_x/Au contacts

In order to prepare electrodes for the local deposition of 2D perovskite, physical vapour deposition (PVD) through a shadow mask is employed. In this way a NiO_x/Au electrode can be deposited on the quartz substrate in an interdigitated fashion as shown in Figure 6. The use of a shadow mask is facile, since no lithographic steps have to be taken. This means that multiple electrodes can be prepared during one deposition cycle without need for etching or lift-off. For the electrochemical deposition step a continuous electrode should be deposited, which can also be done easily with the shadow mask. However, the precision of the dimensions of the deposited features depend on the manufacturing process of the shadow mask. The mask used in this work was made laser cutting, of which the features are limited to a range of ~0.2 mm. Therefore the edges of the mask are not completely sharp on µm scale. Another limitation that is of influence on the deposition feature sharpness is the distance between the mask and the substrate. When substrates are put in a sample holder for PVD they might not be in direct contact with the shadow masks, which results in an effect called overspray. With this overspray an uneven thin film with sloped edges are formed, changing the total area of the deposited film.

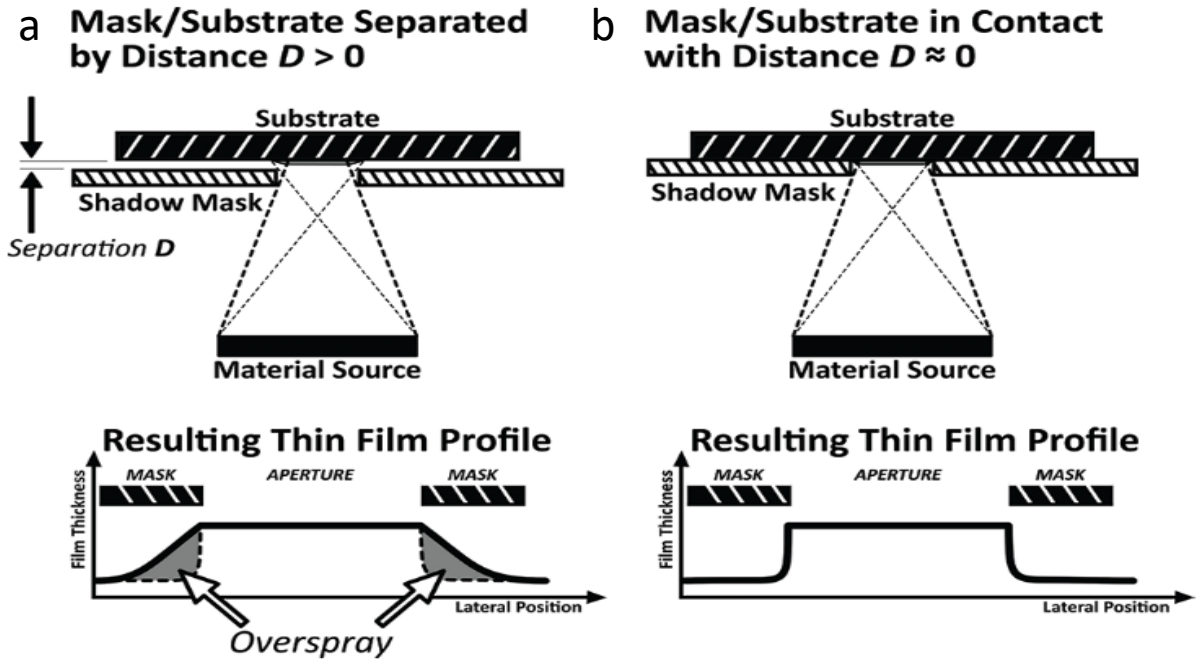

***Figure 6**: Thin film height profile for deposition with shadow mask separated by distance D from substrate (left) and shadow mask in close contact with substrate (right). Figure from: Fisher et al., 2016.*[54]

The initial experiments were performed on bulk NiO_x/ITO substrates to optimise the electrodeposition and conversion of PbO_2. Additionally, the transparency of ITO enables backside illumination of the bulk samples to help in the characterisation of the 2D/3D junction with photoluminescence (and absorption) measurements.

The insights obtained from the production of the bulk samples were finally transferred to the sample of interest i.e the interdigitated NiO_x/Au contacts on top of a non-conductive quartz substrate. In Figure 7a a schematic overview of an interdigitated back-contact device is shown. The blue circle indicates the region that is exposed to the electrolyte solution during the electrochemical deposition. Furthermore, the dimensions of the interdigitated 'fingers' are shown as well as the mask design on the back of the electrochemical cell (Figures 7b and 7c).

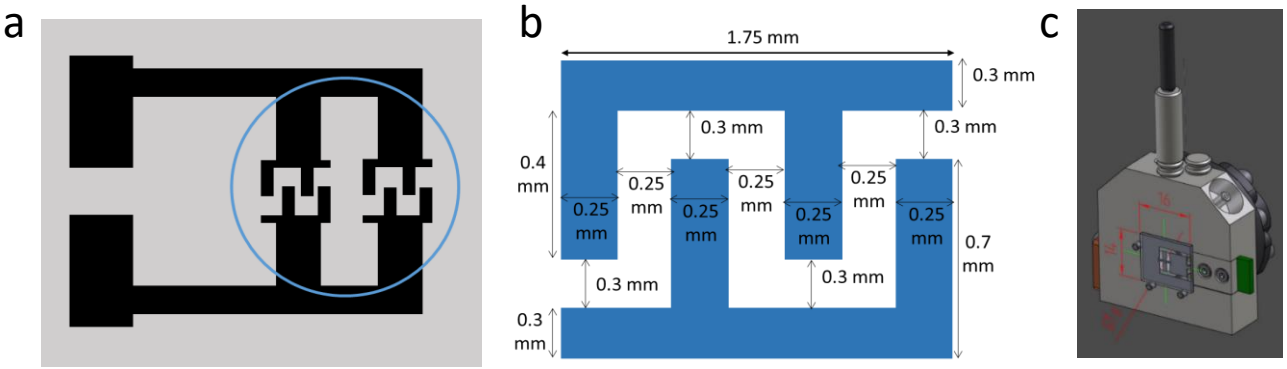

***Figure 7**: schematic overview of IBC sample (a), with the dimensions of the interdigitating area (b) and electrochemical cell mask design (c). The blue circular area in (a) shows the deposition area for electrochemistry.*

2.3 Electrochemistry

The first step in the sample synthesis is electrochemical deposition of PbO_2. In electrochemical deposition redox reactions are facilitated due to electrically induced charge transfer between the interfaces of a conductive environment, which is provided by a liquid electrolyte and two conductive solids that act as electrodes. On either of the two electrodes a reduction or oxidation reaction can take place. In a conventional electrochemical setup, the desired reaction takes place at the working electrode. The counter electrode supplies or extracts the electrons needed in the reaction. The counter electrode is mostly made up of a material that is inert and does not corrode (i.e. graphite, gold, or platinum). Furthermore, the counter electrode generally contains a higher surface area than the working electrode to ensure enough current can be generated. An additional reference electrode can be added to measure the potential between the electrolyte and the working electrode. This reference electrode must have a stable, well-known potential. Ag/AgCl is an almost ideal non-polarizable electrode that can be used for this purpose, due to its low half-cell potential and very low impedance.[55] In this research an electrochemical cell with a three-electrode setup was used that was designed and used in previous research by Alarcon-Llado et al. and shown in Figure 8.[56] The three electrodes used here are a platinum mesh as counter electrode, an Ag/AgCl (leak less miniature ET072-1) as reference electrode and the conductive samples as working electrodes.

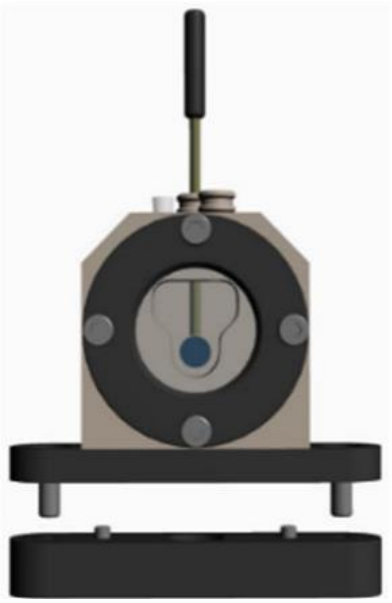

***Figure 8**: Electrochemical Cell used in this research. Figure from: Alarcon Llado et al., 2020.*[56]

In this work, we aim to deposit lead dioxide since this is a naturally formed product during oxidation that is very workable in ambient temperatures and ambient pressures and it is easily converted into perovskite. Lead dioxide is an inorganic compound that is found in two polymorphic structures (Figure 9): α-PbO_2, which possesses an orthorhombic structure and β-PbO_2, which possesses a tetragonal, rutile structure. Both consist of a lead(IV) centred ion in a distorted octahedron of oxygen atoms. The polymorphs vary due to a difference in the octahedra packing. In β-PbO_2 the neighbouring octahedral share opposite edges, resulting in linear chains. In contrast, neighbouring octahedra in α-PbO_2 share non-opposite edges, leading to the formation of zig-zag chains.[57]

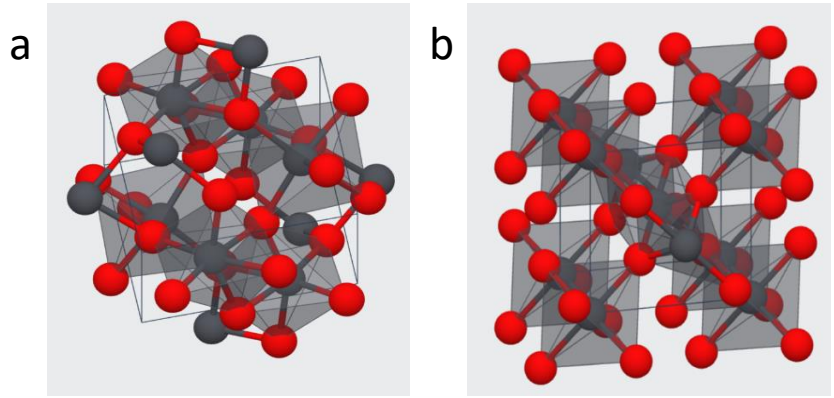

***Figure 9**: crystal structures of orthorombic α- (a) and tetragonal β- (b) phases of lead dioxide. Figure from: Persson, 2014*[58]

The formation of lead dioxide has been widely studied and the most accepted mechanism of PbO_2 nucleation and growth was proposed by Velichenco et al., which involves the adsorption of OH on the substrate as a key intermediate.[59] When using a lead nitrate electrolyte the lead dioxide electrodeposition follows the following three step pathway:

$$H_2O \rightarrow OH_{ads} + H^+ + e^- \quad [1]$$

$$Pb^{2+} + OH_{ads} \rightarrow Pb(OH)^{2+} \quad [2]$$

$$Pb(OH)^{2+} + H_2O \rightarrow PbO_2 + 3H^+ + e^- \quad [3]$$

The first step of this mechanism is the splitting of the water molecule and the formation of oxygen-containing species such as adsorbed OH (1), followed by an intermediate complexation between the lead species and the adsorbed OH, forming a soluble cationic intermediate species containing lead(III) (2). This lead(III) species is subsequently oxidized to lose another electron to form a molecule of PbO_2 on the working electrode (3). To monitor the progress of the electrochemical reaction a potentiostat was used, a device that can control the potential or current of an electrochemical system. Two different applications of the potentiostat were used in this work; cyclic voltammetry and chronoamperometry.

Cyclic voltammetry is a technique that can provide insights in both the number and nature of redox reactions taking place in an electrochemical system. The potentiostat applies a triangular wave potential to the system sweeping the potential back and forth between two potentials E1 and E2. The potential variation over time is called the scan rate. During this potential sweep the current response is measured. When a certain potential threshold is reached (the onset potential), the current response will go up at which point the activation barrier is crossed and the oxidation (or reduction) reaction can take place. When the reaction is reversible reduction (or oxidation) occurs during the reverse sweep. A typical CV curve for PbO_2 electrodeposition can be seen in Figure 10.[60] There, two cathodic current peaks are observed on the negative scan (R_1 and R_2) of the voltammogram, corresponding to Pb (IV) and Pb (III) species reduction. In the positive scan of the cyclic voltammogram, two anodic current peaks are observed (A_1 and A_2). These peaks correspond to the oxidation potentials of Pb(II) species (equation (2)) and Pb(III) species (equation (3)), respectively.

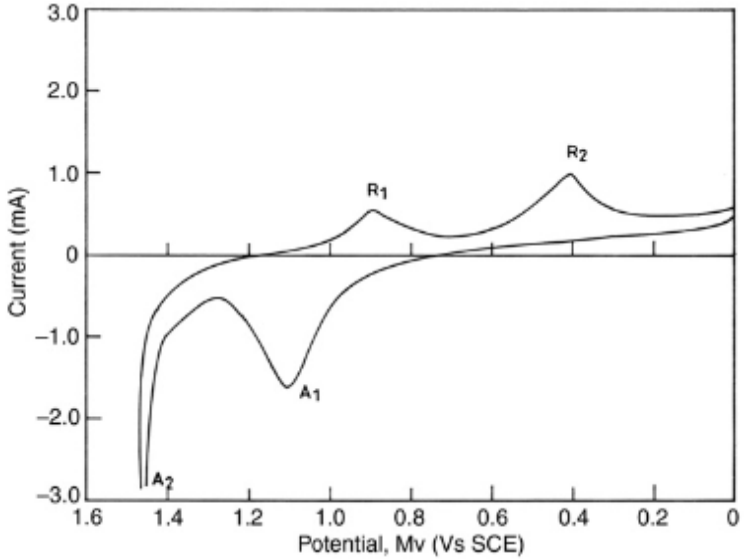

***Figure 10**: A typical cyclic voltammogram of electrodeposition of PbO_2 from 0.1 M $Pb(NO_3)_2$ solution onto a copper substrate. Figure from: Kim et al, 2007.* [60]

Chronoamperometry (CA) is a technique which, in contrast to cyclic voltammetry, employs stepwise voltammetry with instantaneous switching of the potential. When this potential is kept constant over a certain time a current response like in CV can be measured. An example of a typical CA curve is seen in Figure 11. With this technique high charging currents are generated, which decay exponentially over time. When the area of this I-t curve is integrated the total charge that is transferred to the working electrode is obtained. By using Faraday's law (Q = nF) it is then possible to calculate the theoretical conversion of the intended electrochemical deposition. In this work, CA is used to control the growth of the PbO_2.

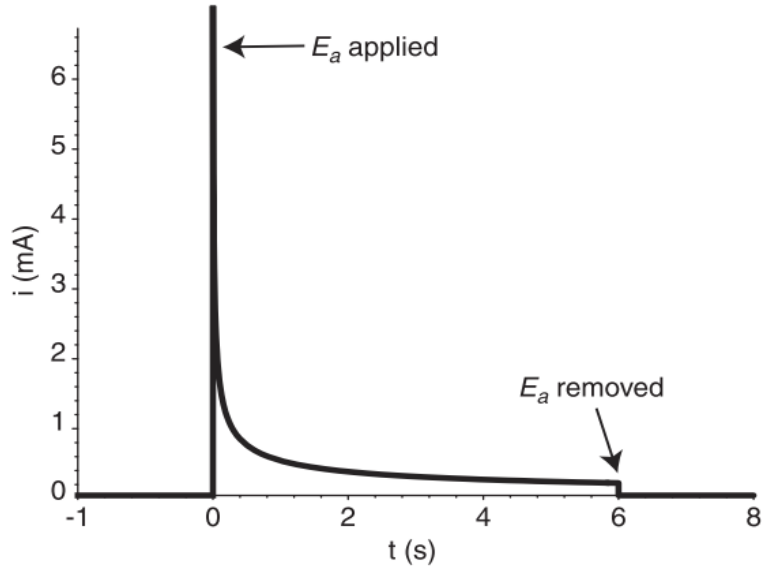

***Figure 11**: Ideal chronoamperometric curve, with a current response (in mA) as a function of E_a. Figure from: Brown et al., 2016.[61] After initial application of the voltage E_a, a high current is generated immediately that decays exponentially until E_a is removed.*

A constant anodic potential (overpotential) is applied to the system based on the highest oxidation peak found in the CV curve (A2). Due to this anodic overpotential the equilibrium is pushed towards the oxidation reaction and PbO_2 is deposited on the substrate. By changing the time that the overpotential is applied the total amount of PbO_2 deposited can be controlled.[59] It was found that adhesion, surface morphology and ratio of α/β forms can be influenced by many parameters, including: substrate choice, pre-treatment of substrate surface, pH ranges (alkaline or acidic), electrolyte anion, lead(II) concentration, current density, deposition potential, charge density.[59,62–70] In this work nitrate electrolytes with a low pH have been employed to deposit lead dioxide on pre-treated nickel oxide substrates, since nitrates are an often used electrolyte that do not require many additives. Typically, using these conditions would result in lead dioxide deposition with a high proportion of the β-phase.[49] Although the β-phase is not a requirement for the conversion to the perovskite. According to Popov et al. the uniformity of the film coverage is more important.[45]

2.4 Chemical Vapour Deposition.

As shown above the electrodeposition method is used to deposit the lead precursor films. In turn, the films can be chemically converted into the intended final perovskite by different two-step conversion processes.[45,47–49] Conversion of electrodeposited lead dioxide to perovskite was first shown by Chen et al. in 2015.[47] Here a two-step dip coating conversion with hydrogen iodide (HI) and methylammonium iodide (MAI) was employed. In the first step the HI is used to convert the deposited lead dioxide film to lead iodide. In a subsequent dip coating step the lead iodide film is converted to methyl ammonium lead iodide (MAPI). The HI is believed to reduce the Pb(IV) species in PbO_2 to Pb(II) in PbI_2 with the following equation:

$$PbO_2(s) + 4\,HI(g) \rightarrow PbI_2(s) + I_2(g) + H_2O \qquad [4]$$

This method was adapted by Popov et al. to convert the lead iodide film to perovskite. Here, instead of the dip coating conversion, chemical vapour deposition (CVD) of MAI was employed.[45] CVD is a technique in which an organo-halide material (e.g. FAI, MAI, PEAI, butylammonium iodide (BAI) or related bromine analogue) are sublimed and its vapour is transported to the desired substrate by an inert carrier gas (e.g. Ar, N_2).[71] At the substrate this vapour reacts with the pre-deposited precursor layer (e.g. metal halide, metal oxide). This technique usually employs low-vacuum conditions, during which lower temperatures are needed to reach fast sublimation of the organo-halide compound than during ambient pressure vapour deposition. In a typical CVD process a tubular flow reactor is used because these allow for a simple and customizable experimental setup. These reactors are often composed of a long quartz tube surrounded by a heating furnace that offers a controlled temperature zone (Figure 12). Generally, the tube contains a carrier gas inlet on one end and a vacuum pump outlet on the other end. Understanding and controlling the nucleation and growth mechanisms of perovskite films in vapour deposition techniques is equally as important as for solution-based processing. The growth process is influenced by parameters such as deposition chamber pressure, substrate temperature, substrate material surface properties and morphology, as well as carrier gas flow rate.

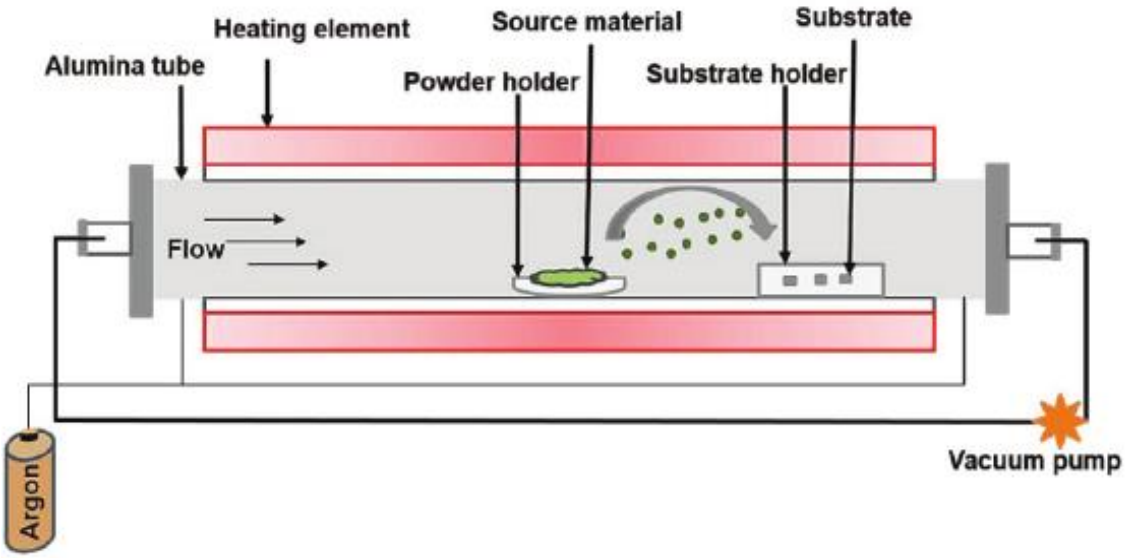

***Figure 12**: Illustration of carrier gas assisted CVD setup in a tubular furnace. Figure from: Sberveglieri et al., 2015.*[72]

The aforementioned processes all used HI vapour, although working with HI adds complexity to the experiment and is usually avoided due to toxicity.[46] Therefore Lee et al. developed a method that did

not involve the intermediate step of lead iodide formation. Here the electrodeposited PbO_2 is first reduced to PbO by annealing in a H_2/Ar gas atmosphere, since it was believed that this would lead to smoother film formation.[45,50,73,74] This PbO layer is then converted to MAPI with the CVD technique. The proposed mechanism of conversion comprises of two steps (eqs. 5-7). During the sublimation in of CH_3NH_3I, HI and MA are formed (eq. 5). The HI can then react with the PbO in a ligand exchange reaction to form PbI_2 and water (6). Subsequently the formed PbI_2 can be converted to perovskite by direct reaction with MAI vapour (7). This mechanism has been proposed by Cui et al [44]

$$CH_3NH_3I \rightarrow CH_3NH_2 + HI \quad [5]$$

$$PbO + 2\,HI \rightarrow PbI_2 + H_2O \quad [6]$$

$$PbI_2 + CH_3NH_3I \rightarrow CH_3NH_3PbI_3 \quad [7]$$

However, recently Heydari et al. have shown that this reduction step was not necessary to convert PbO_2 to perovskite. In their process an electrodeposited PbO_2 layer was converted to $MAPbBr_3$ by direct evaporation of MABr on the substrate.[75] They propose a similar two step conversion. Due to the direct conversion without need for extra reduction steps this CVD method was adapted in this work to directly convert a PbO_2 film to $(PEA)_2PbI_4$. Direct electrodeposition of PbO was not performed since this would require unstable hydrogen peroxide solutions, or dimethyl sulfoxide addition, elevated temperatures and degassing of the solution to remove dissolved oxygen.[45]

2.5 3D perovskite deposition

Three different methods for the formation of the 2D/3D heterojunction were used. The first is dynamic spin-coating, where the 3D precursor solution was spin-coated on top of an existing 2D perovskite sample. However, the use of solvents will have influence on the 2D perovskite layer by (partial) dissolution of this layer. Therefore two different solvent free pathways to create a clean 2D/3D heterojunction have been investigated recently to deal with this problem: multi-source thermal evaporation of a 2D/3D heterojunction[36–38] and solid-phase in-plane growth.[39] After various trials on all three methods, the mutli-source thermal evaporation was chosen as the technique to form a thin 3D perovskite film on our 2D junction. In multi-source thermal evaporation all precursors are vacuum evaporated with independent heating of every precursor. When optimized, this technique leads to high control of film deposition thickness and composition.

Since a lot of steps have to be taken in this project to form the final samples a schematic overview of the bulk sample formation is shown in Figure 13. In three steps a 2D/3D heterojunction will be formed. By first electrodepositing PbO_2 on NiO_x/ITO substrate, which is converted by CVD in the next step. The final step is to deposit a 3D perovskite layer on top of this by multi-source thermal evaporation.

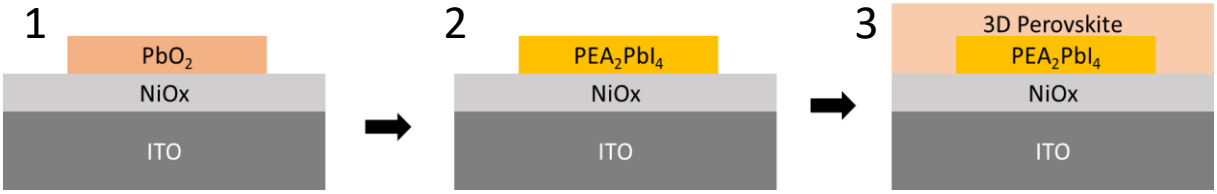

***Figure 13**: Schematic formation of bulk 2D/3D heterojunction samples by (1) PbO_2 deposition, (2) CVD conversion to 2D perovskite: PEA_2PbI_4, (3) 3D perovskite deposition.*

When these bulk samples are formed the knowledge will be transferred to the patterned substrates In Figure 14 the 7 subsequent steps with which the patterned device is created are shown. The first step is to clean a quartz glass substrate, on which a patterned contact is formed by sequential electron beam deposition of titanium (2), gold (3) and nickel oxide (4). On this patterned contact the electrochemical deposition of PbO_2 occurs (5), which is converted to $(PEA)_2PbI_4$ (6). In the final step multi-source thermal evaporation is used to create the final device.

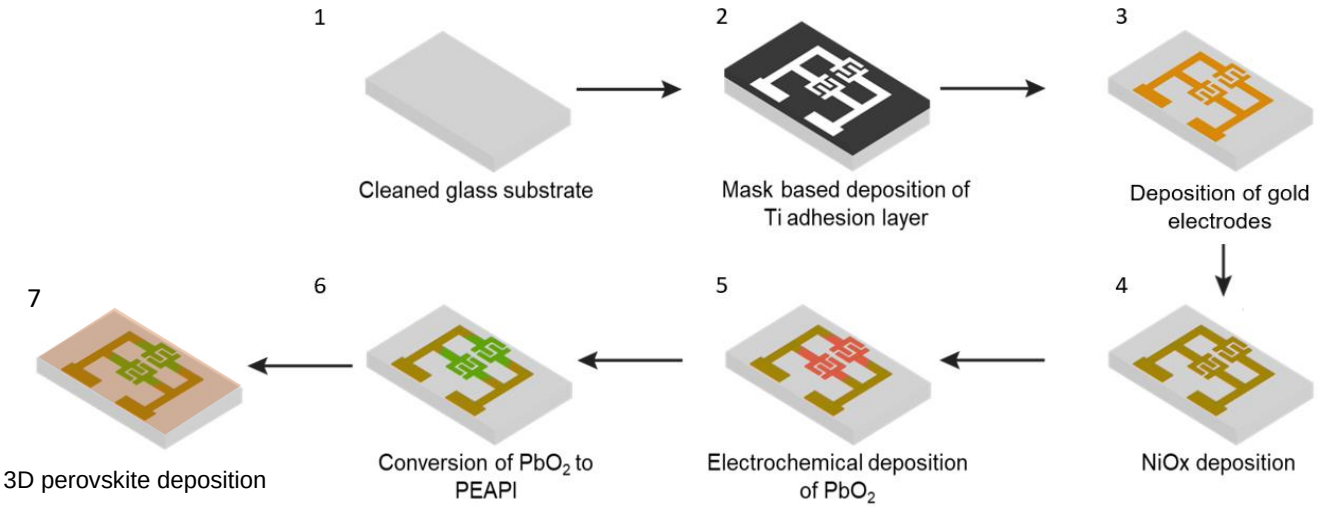

***Figure 14**: Synthesis plan of IBC samples. On a clean glass substrate (1) a titanium adhesion layer (2) , gold electrodes (3) and a nickel tranpsort layer are deposited sequentially by e-beam deposition with a shadow mask. This nickel layer is annealed to form nickel oxide (4). During electrochemical deposition a lead dioxide layer is formed on a selective area of the NiO_x/gold contact (5). This is converted to PEA_2PbI_4 by CVD (6). In the final step a 3D perovskite layer is deposited on top of the sample (7).*

3. Results & Discussion

In this section the results of the research will be discussed. The goal is to use electrodeposition for the local formation of 2D perovskite to use this as a passivation layer underneath 3D perovskite. This will be started with the 2D formation of the bulk samples, electrodeposition of PbO_2 will be discussed, followed up with the conversion to 2D perovskite by CVD. The translation of these findings to the patterned gold substrates is shown next. After that the heterojunction formation will be discussed. This section finishes with TRPL measurements TRPL to see how heterojunction influences charge carrier dynamics in 3D perovskite.

3.1: Electrodepostion of PbO_2 on NiO_x/ITO films

To confirm that lead dioxide could be grown on a NiO_x layer a first electrodeposition was performed on a substrate with a thin layer of NiO_x (~15 nm) on ITO. Formation of a dark brown film was observed. The CV curve of this deposition shows two peaks at 0.5V (R_1) and 1.3V (R_2), as shown in Figure 15. These peaks could be attributed to the expected oxidation of Pb(II) to Pb(III) (R_1) and subsequent oxidation to Pb(IV) (R_2).

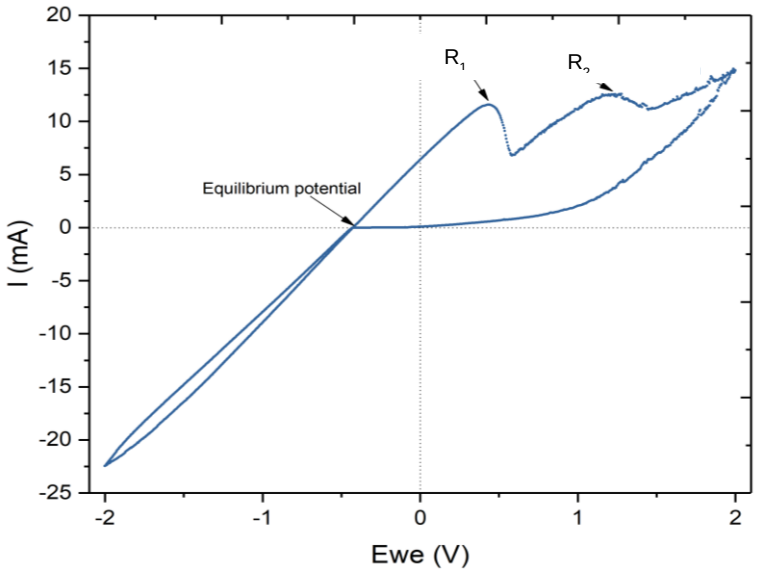

***Figure 15**: CV curve of 0.1M $Pb(NO_3)_2$ on NiOx/ITO*

Based on the CV curve, the deposition potential for CA was set to 1.5V vs Ag/AgCl. With this potential a deposition series was performed where CA time was varied. The circular deposition area of the sample turned from colourless to dark brown after the electrochemical deposition. The current vs. time graph of the deposition is shown in Figure 16. The graph shows an initial peak in the current of 5 mA/m^2, after which the current follows an S-curve. The increase of current density after t=20 is likely caused by dendritic growth, due to changes in the resistance of the material.[76] This change can come from increased electrolyte temperature, increase in true electrode surface area or an unsteady mixing regime. Therefore it only occurs after a prolonged deposition time.

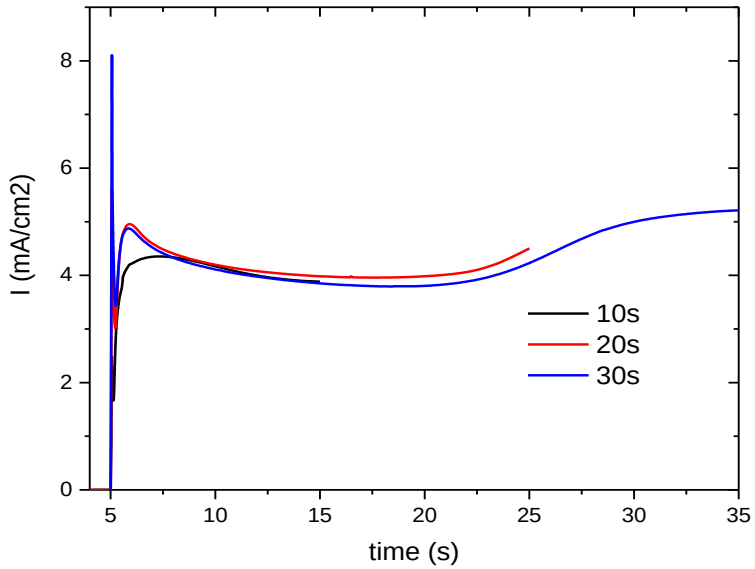

***Figure 16**: Chronoamperometry graphs of electro-deposition on NiO_x/ITO substrates for different deposition times at 1.5V vs Ag/AgCl.*

In the SEM images in Figure 17a it can be seen that there is a boundary between the area where PbO_2 has formed and the underlying NiO_x/ITO can also be seen. This is due to the circular deposition area of the electrochemical cell. In Figure 17b it is shown that a continuous film is formed, the grains are roughly 50-100 nm in size.

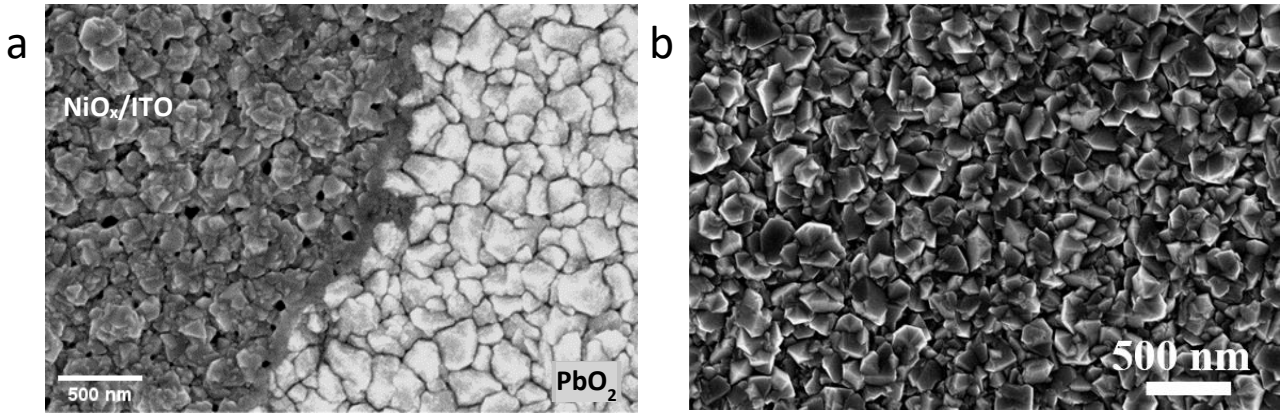

Figure 17: SEM images of PbO_2 sample with (a)boundary between PbO_2 and NiO_x/ITO and (b) central area of the film.

As shown in the XRD graph in Figure 18 two distinct phases of PbO_2 are present in the film. The peaks at 28.0 and 30.2 show the presence of the α-phase and the peaks at 25.5, 32.1, 36.3 and 49.2 indicate the presence of the β-phase of PbO_2. No information of the proportion between the two can be taken from the XRD spectra. The XRD spectra confirmed that PbO_2 film formation was possible on a NiO_x/ITO substrate. When films with lower deposition times were fabricated only the (110) peak could be found on the XRD spectrum, which could imply that the films were too thin for the machine to pick up any signal of the other orientations. However, visually the brown colour of the film could still be seen. Therefore, based on the combination of the XRD spectra, optical observations and CA data it was assumed that the deposited films were composed of PbO_2.

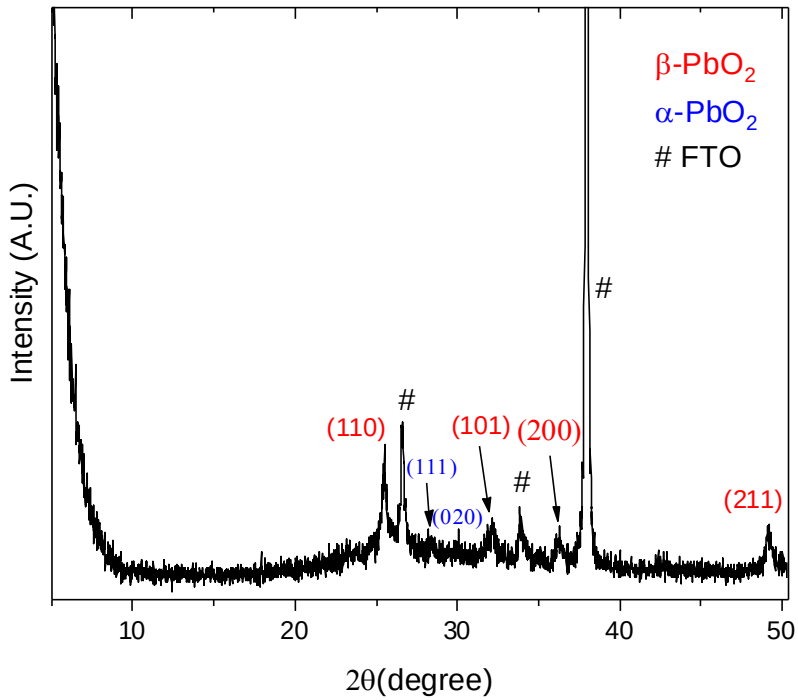

***Figure 18**: X-ray diffractogram of PbO_2 deposited film. Different lead dioxide phases are highlighted in blue and red.*

In this section it has been shown that PbO_2 could be deposited electrochemically on top of a NiO_x/ITO substrate, confirmed optically and by XRD and CA data. A deposition time of 5 s and accompanying

thickness of 37 nm PbO_2 was chosen as final parameter. Therefore the next step in the research could be taken, conversion of PbO_2 to the 2D perovskite $(PEA)_2PbI_4$.

3.2 PbO_2 conversion to $(PEA)_2PbI_4$ by Chemical Vapour Deposition

CVD of PEAI was used to convert the PbO_2 films to $(PEA)_2PbI_4$. For this conversion some parameters were optimized (i.e. gas flow, pressure, temperature and conversion time). The gas flow was set to 35 ml/min, which was the lowest rate at which the Nitrogen or Argon flows where stable. In literature no reports were found on the CVD of PEAI. However, MAI has been evaporated at pressures below 0.7 bar and temperatures of 170 °C.[77,78] PEAI is a bigger molecule with a phenyl moiety instead of a methyl group, which means that the temperature of evaporation is higher than that of MAI. To help the diffusion of the heavier PEAI the pressure was lowered and the temperature was increased. Therefore, pressure was set to 70 mbar and the temperature to 180 °C. Furthermore the evaporation time was set to 6h. In the conversion of PbO_2 to MAPI the conversion time was set to 2h, however this was a conversion from PbI_2 to MAPI, and not a direct conversion from PbO_2. It was expected that the conversion from PbO_2 to PbI_2 would take some time before the conversion to PEA_2PbI_4 could start. In the first few stages it was noticed that the conversion did not occur in one step from PbO_2 to $(PEA)_2PbI_4$.

After 6h of CVD The sample turned from brown to yellow by eye and when illuminated with a 425 nm UV lamp no luminescence was shown. This indicated that there might have been formation of PbI_2 instead of the desired 2D perovskite. Therefore a second CVD step was performed with the same parameters as the first step. This resulted in a differently shaded yellow film, which showed green luminescence under illumination with the 425 nm UV lamp. The XRD spectrum in Figure 19 shows that after the first CVD conversion a peak at 12.7 2θ is observed, which is indicative of PbI_2 formation.[79] After the second CVD conversion a (002) peak of the converted PbO_2 film and its repetitions can be seen, which suggests $(PEA)_2PbI_4$ formation.[38,80]

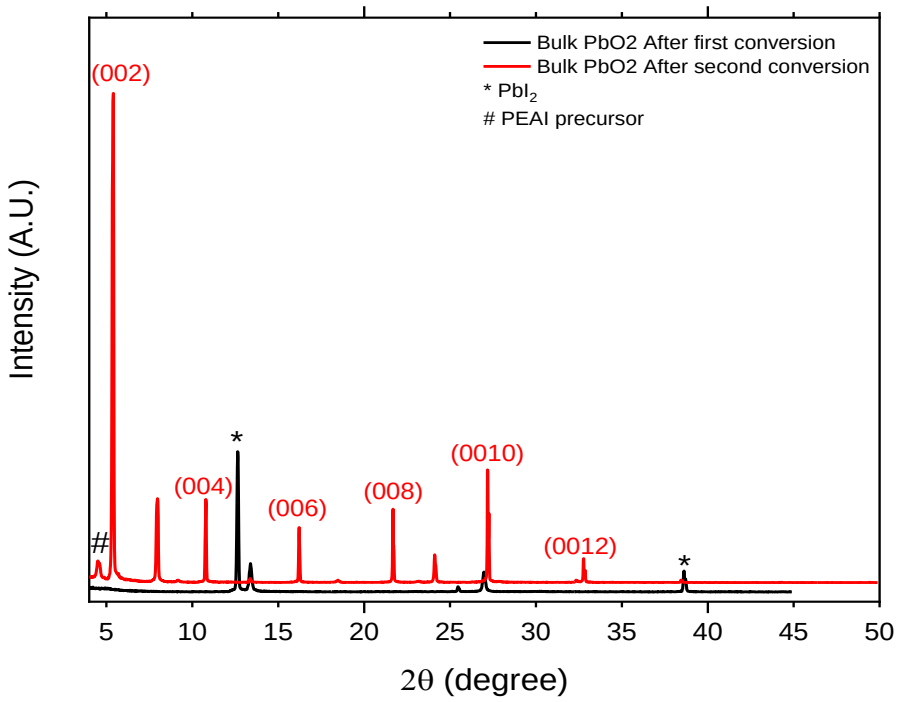

***Figure 19**: X-ray diffractogram of PbO_2 converted film on bulk NiO_x/ITO.*

In the UV-VIS absorption spectrum after the second conversion the peak at 520 nm can be attributed to $(PEA)_2PbI_4$ and in the PL spectrum the peak at 525 nm is characteristic for $(PEA)_2PbI_4$ 2D perovskite emission (Figure 20).[52] In the PL map of Figure 21 it can be seen that the film has a gradient of intensity

at 525 nm. This could indicate that there are thickness differences across the sample or a difference in PLQY for different regions in the sample due to a different morphology, which could induce trap states.

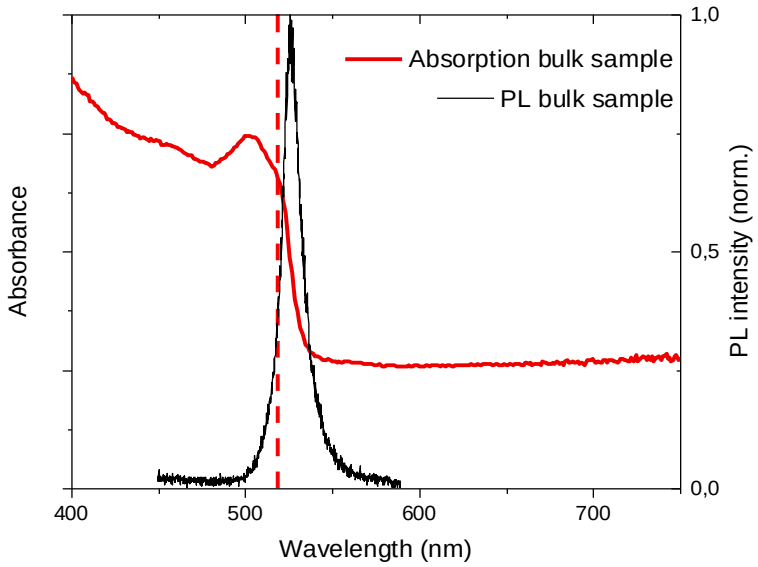

***Figure 20**: UV-VIS absorption and PL (normalized) spectra of converted bulk sample. Dashed lines show reference absorption of $(PEA)_2PbI_4$ at ~520 nm.*[52]

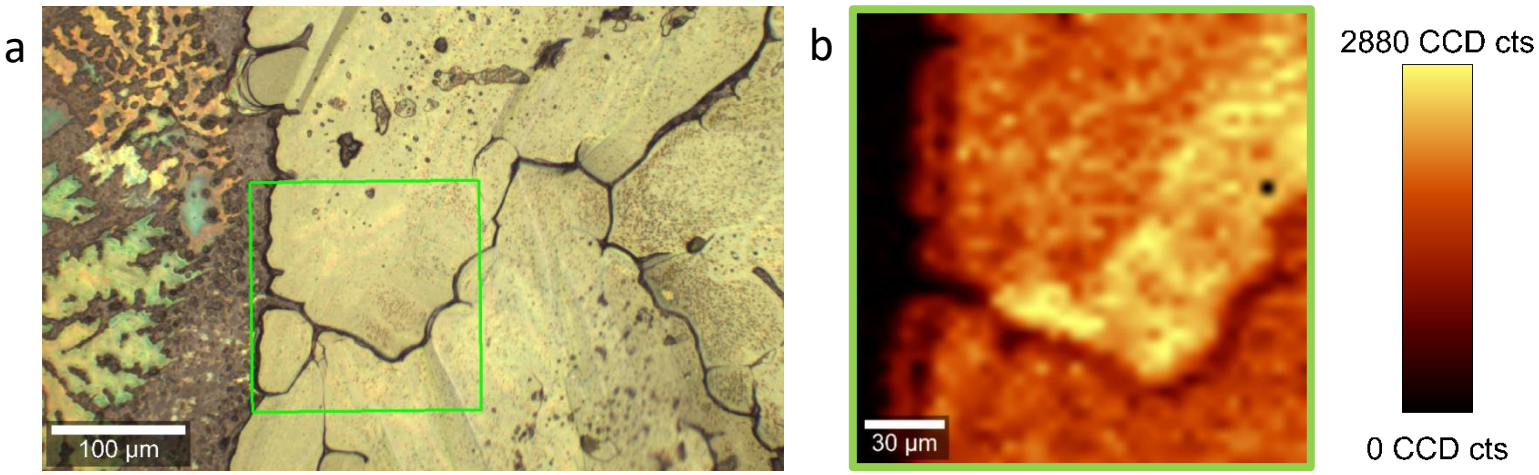

***Figure 21**: PL map of an area at the edge of the sample. Optical image of the area (a) and PL map of the highlighted green area (b). CCD counts were plotted for a wavelength of 525 nm.*

When thickness of the films was measured with a profilometer very large differences in thickness were found. The base of the measured areas of the bulk sample was close to 2 microns. Height differences could occur due to formation of other structures or due to the gaps in between the grain clusters. The average film thickness is shown in Table 1 and increased up to a factor 13.5 when compared to the thicknesses of the PbO_2 films. For conversion of PbO_2 into 3D perovskite films expansions of 4.5 times have been reported and PbO_2 to PbI_2 conversion the thickness generally doubled.[78] Since the 2D perovskite is bulkier than the 3D perovskite, especially in *n*=1 conformation, the factor 13.5 increase seems plausible, yet unlikely.

Table 1: Thicknesses of PbO_2 films before and after conversion to 2D perovskite based on different electrodeposition times.

Deposition Time (s)	Film thickness after EC (nm)	Film Thickness after CVD (nm)
50	300	2000
30	120	1400
20	68	780-800
10	37	500-750
5	24	-
3	17	-
2	12-20	-

After the first conversion step it was found that the CVD resulted in plate like structure formation (Figure 22b) In the SEM images of Figure 22c it can be seen that large plates of material are formed. In Figure 22d a zoomed in view shows that in between the gaps of these plates some smaller plates are formed, stacked on top of each other. On top of the large plates small dots are formed which might possibly be attributed to precursor material recrystallization, for which an XRD peak at 4.5 2θ could sometimes also be seen such as in Figure 19.

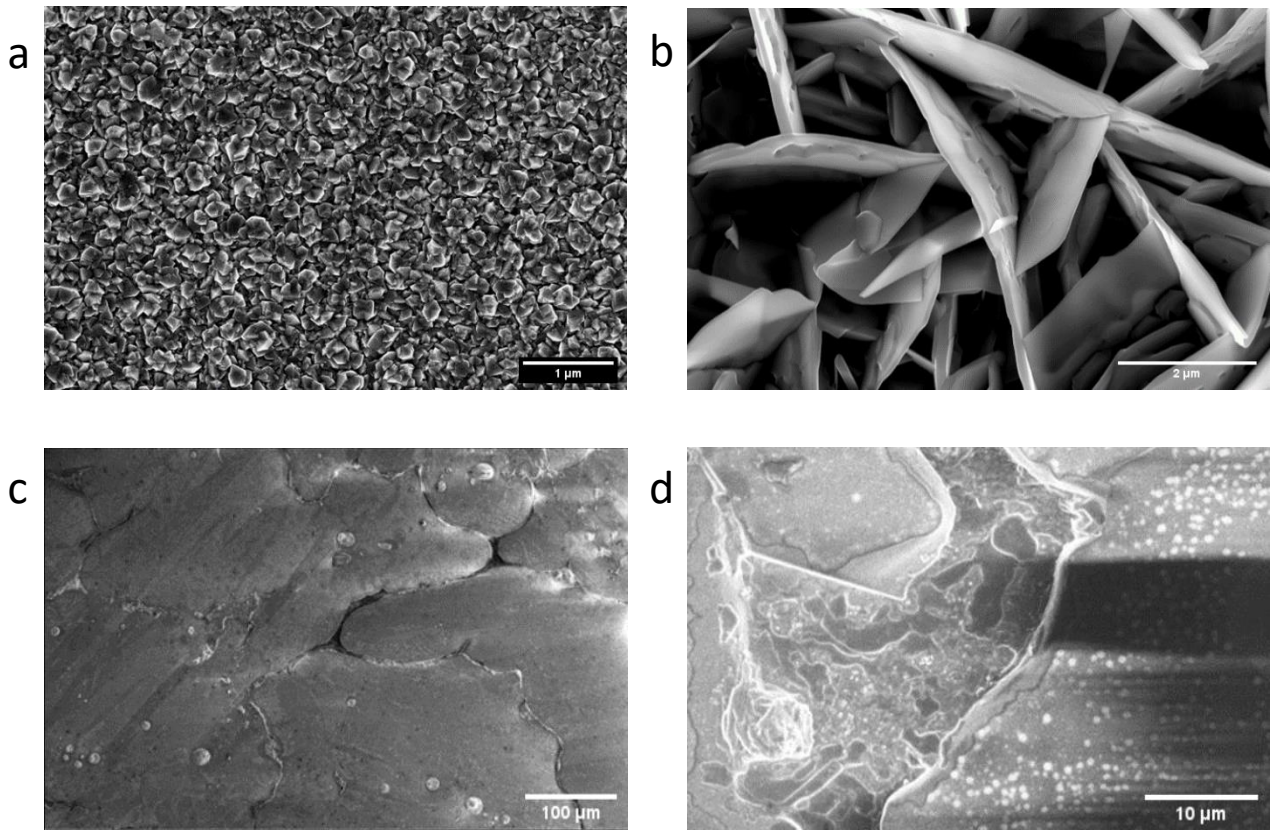

***Figure 22**: SEM images of PbO_2 films before (a) and after a first (b) and second conversion step(c-d).*

One way to explain the specific morphology of these films is Volmer-Weber growth (Figure 23a), which is the typical growth mode for perovskite films from the vapor phase.[81] In Volmer-Weber growth small molecular clusters are directly nucleated on the substrate, therefore forming different islands which can differ greatly in height. This growth can occur when deposited molecules are more strongly bound to each other than to the substrate. Although, since it looks like there are some layers underneath the height differences it might be more likely that Stranski-Krastanov growth has taken place (Figure 23c). In this growth type a combination of layer by layer growth and island growth occurs. These growth modes can be induced by changing processing parameters.[81] The specific dynamics of the growth mode is difficult to be understood in processes that include more steps than just vapor deposition, as is the case for this research. Inter-diffusion processes may also occur during the perovskite growth or the morphology of the PbO_2 precursor film could influence the growth mode of the perovskite.

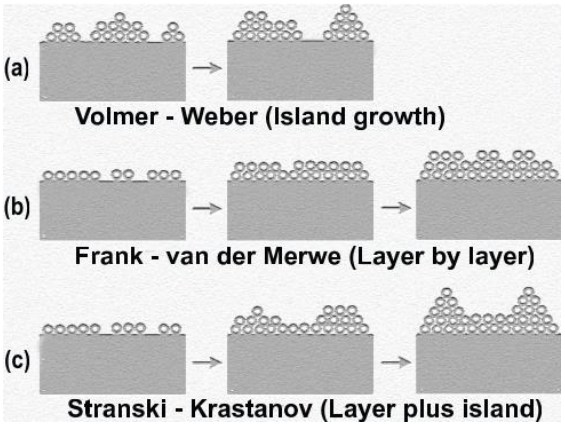

***Figure 23**: Cross sectional views of three primary modes of thin-film growth. (a) Volmer-Weber or island growth (b) Frank-van der Merwe or layer by layer and (c) Stranski-Krastanov or layer plus island. Different surface coverage is gained from each technique with different uniformities. Figure from: Perez, 2018.*[82]

With the combination of the XRD, UV-VIS and PL graphs and the SEM images it has been shown that the PbO_2 thin film has been converted to $(PEA)_2PbI_4$ in two CVD steps. With conversion to PbI_2 during the first CVD step and full conversion to $(PEA)_2PbI_4$ after a second step. This implies that a similar mechanism could take place as in the conversion from PbO_2 to MAPI (section 2.4). A proposed mechanism for 2D perovskite formation is shown below. The first step is sublimation of the PEAI salt (8) and HI and PEA are formed. Here, 4 equivalents of HI reduce the PbO_2 to form PbI_2, iodine gas and water vapour (9). The third step also differs from the mechanism of MAPI formation, since the formed PbI_2 is converted to perovskite by reaction with two equivalents of PEAI instead of one, due to the formation of the 2D structure (10).

$$C_6H_5C_2H_4NH_3I \rightarrow C_6H_5C_2H_4NH_2 + HI \quad [8]$$

$$PbO_2 + 4\,HI \rightarrow PbI_2 + I_2 + H_2O \quad [9]$$

$$PbI_2 + C_6H_5C_2H_4NH_3I \rightarrow C_6H_5C_2H_4NH_2PbI_4 \quad [10]$$

It must be taken into account that this mechanism was not checked by using different conversion times. Furthermore it cannot be excluded that this conversion does take place in one step but the end product turns into PbI_2 due to degradation of the product due to the high temperatures. According to a recent paper by Ham et al. (2021), degradation of the 2D perovskite can occur during CVD if temperatures go beyond a certain optimum.[83] They show that perovskite flakes based on

butylammonium (BA) form the desired cubic phase at 160 °C. However, when temperatures are increased to 170 °C BA was supplied excessively and therefore destroys the rectangular crystal morphology and leave a liquid-like curved morphology. A different set-up for CVD is used there, with three separately controlled temperature regions. The third region is set to 100 °C to provide just enough thermal energy for the large organic moiety to diffuse well on the substrate. In this research, only one temperature region was employed. This meant that the 'growth zone' was roughly the same temperature as the heating zone (i.e. 180 °C). Therefore degradation of the $(PEA)_2PbI_4$ to PbI_2 might occur during the reaction. Additionally, Ham et al. employed a different reaction, namely simultaneous vapor deposition of PbI_2 and BA on a silicon/silicon oxide wafer.[83] Which might mean that they have different reagent interactions. A temperature of 165 °C was suggested for the CVD of PEAI on SnI_4.

In this section it has been shown that PbO_2 films could be converted into $(PEA)_2PbI_4$ with CVD. Based on the SEM, XRD, UV-VIS and PL data it was shown that this conversion could take place, albeit in two steps with PbI_2 formation sometimes. This meant that the knowledge from the bulk samples could be transferred to the patterned substrates.

3.3 Electrodeposition and CVD on patterned NiO_x/Au contacts.

After formation of bulk 2D perovskite films on a NiO_x/ITO substrate the patterning of the 2D perovskite with the aforementioned shadow mask was performed. In Figure 24 the CA graph of PbO_2 deposition on evaporated NiO_x/Au contacts is shown. For different deposition times similar CA curves are observed, when compared to the CA graphs of the bulk PbO_2 deposition the current density has increased. This might be due to the differences in resistance of gold and ITO. No notable increase in current density occurred, which could be attributed to the different electrode or the smaller surface area.

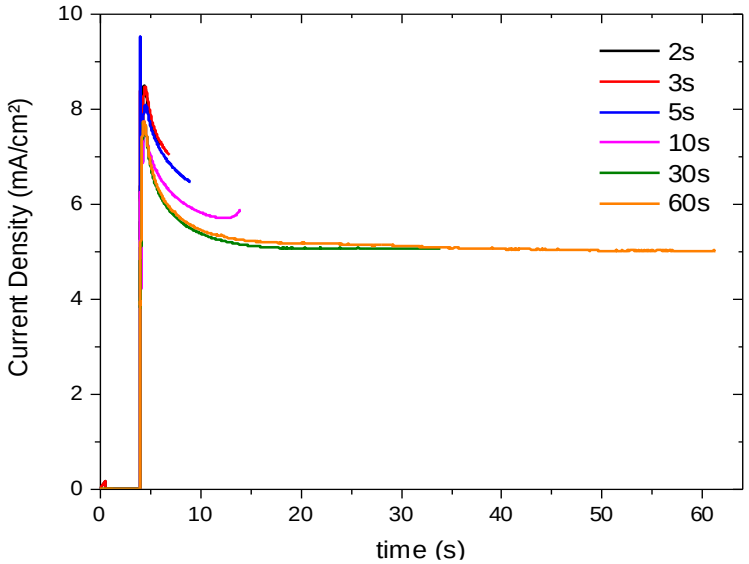

***Figure 24**: CA graph of different deposition times of PbO_2 on top of IBC contacts (NiO_x/Gold) at 1.5V vs Ag/AgCl.*

During the PbO_2 deposition the patterned deposition area changed from gold to a dark brown colour (Figure 25 a+b). In the SEM image it can also be seen that a small grained film was formed on top of the contact (Figure 25e).

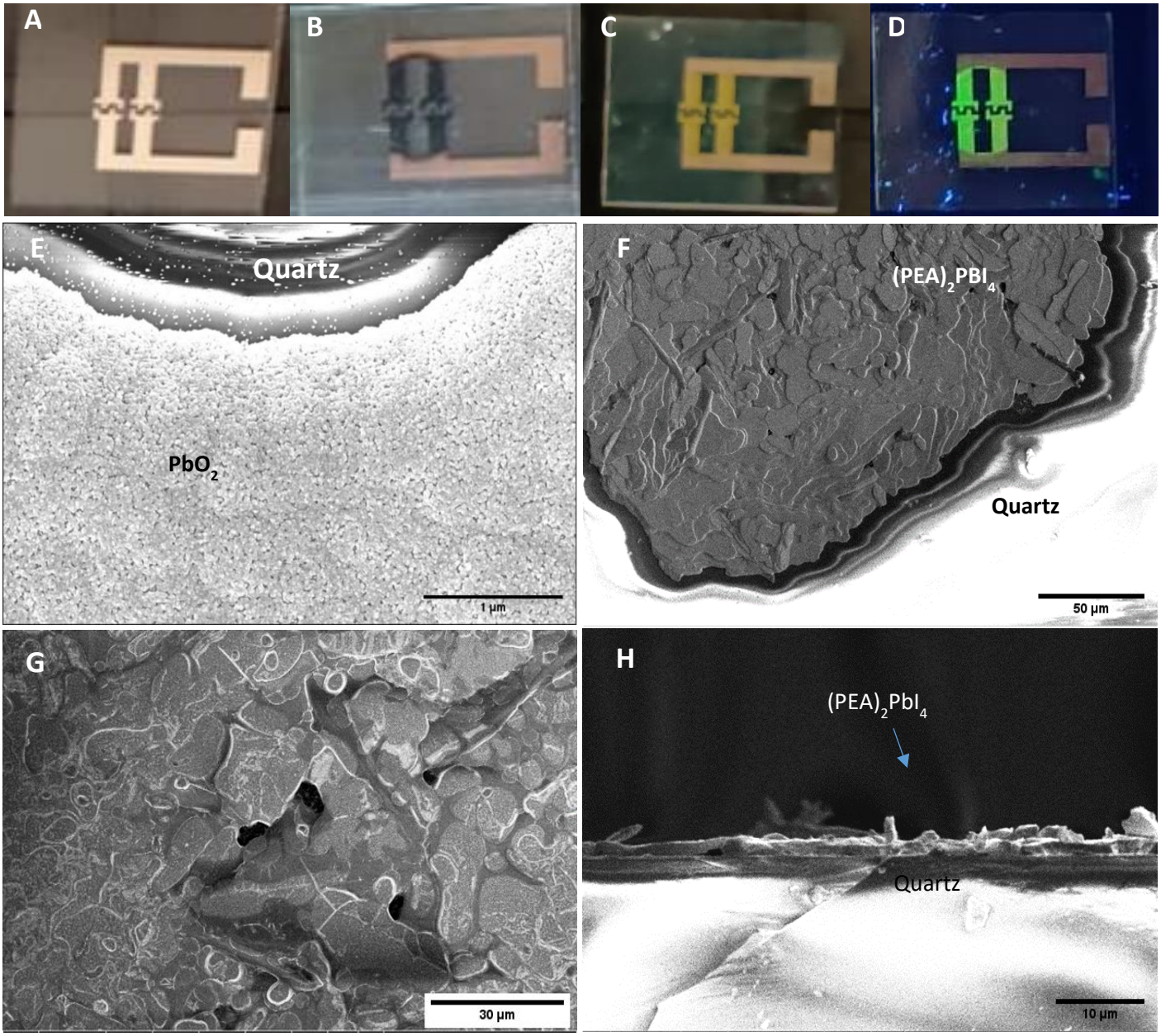

***Figure 25**: Optical and SEM images of NiO_x/gold contact (a), PbO_2 on top of NiO_x/gold contact (b+e), converted $(PEA)_2PbI_4$ film (c+f), under illumination of 405 nm light (d), zoom of centre area of 2D film (g) and of cross-section of a similar sample (h).*

After the electrodeposition step, the patterned film was converted to 2D perovskite with CVD. The brown area turned yellow (Figure 25c) and showed green luminescence during illumination with a 405 nm lamp (Figure 25d). Figure 25f+g show that the formed 2D perovskite has some different morphologies than the converted bulk samples in Figure 19. It can be seen that the growth has been confined on top of the contact area (Figure 25f). However, there are multiple clusters of grains growing on top of or next to each other. Furthermore a large height difference within the sample been observed and some gaps between the different clusters of grains can be observed (Figure 25g). The cross sectional SEM (Figure 25h) shows height differences and some vertical features of the film. This looks similar to the Stranski-Krastanov growth mode mentioned before in Figure 20c.

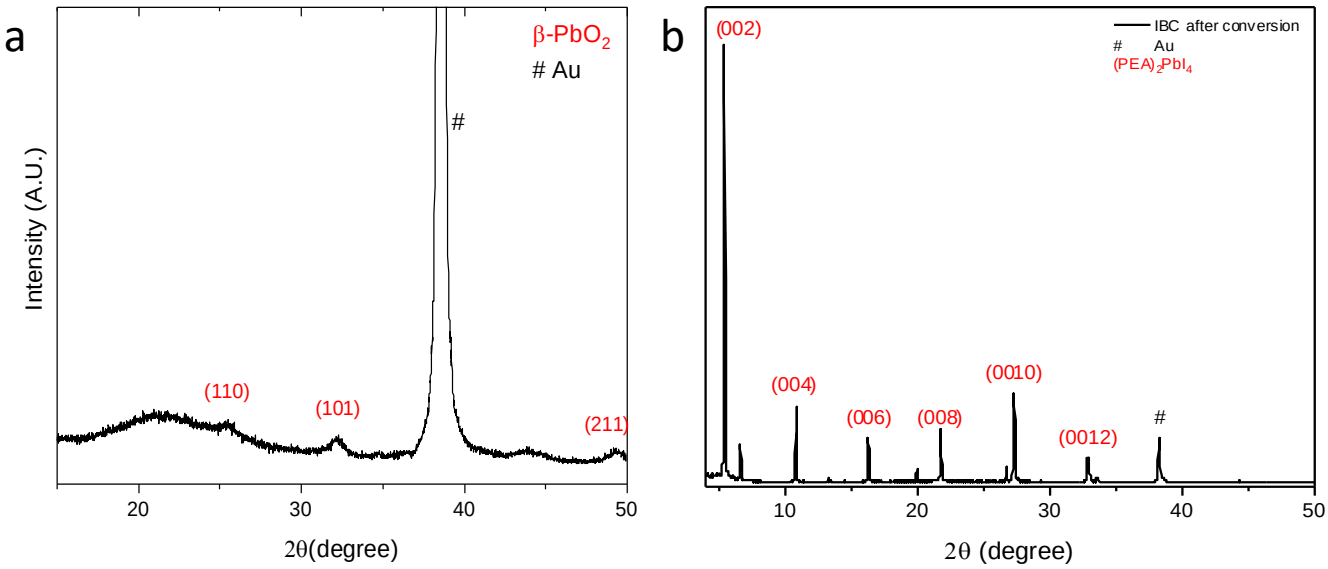

***Figure 26**: X-ray diffractogram of patterned NiO_x/Au contacts with (A) PbO_2 deposited film and (B) converted $(PEA)_2PbI_4$ films.*

The formation of PbO_2 after electrodeposition was also indicated by XRD measurements, the peaks at 25.5, 32.1, and 49.2 indicate presence of the β-phase of PbO_2 (Figure 26A). After CVD conversion a (002) peak and its repetitions can be seen, which suggests $(PEA)_2PbI_4$ formation (Figure 26B). Similar to the bulk samples, the peak at 520 nm in the UV-VIS absorption spectrum after the conversion can be attributed to $(PEA)_2PbI_4$ and in the PL spectrum the peak at 525 nm is characteristic for $(PEA)_2PbI_4$ 2D perovskite emission (Figure 27).[52]

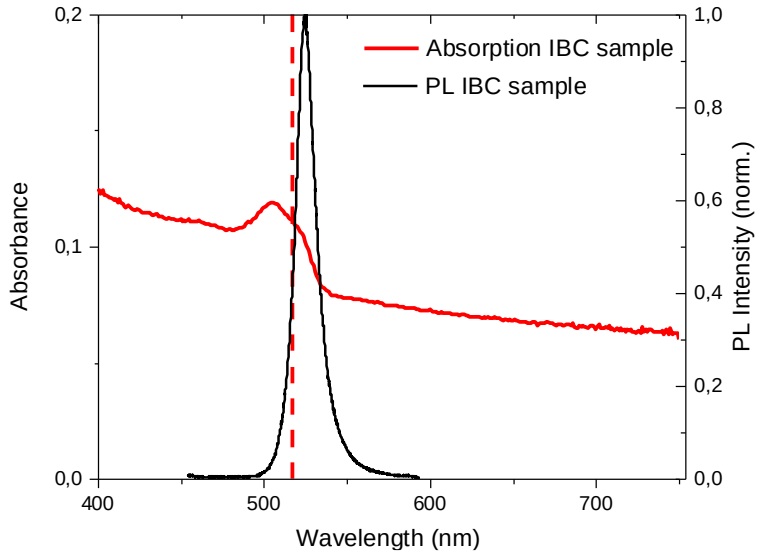

***Figure 27**: UV-VIS absorption and PL (normalized) spectra of converted bulk sample. Dashed lines show reference absorption of $(PEA)_2PbI_4$ at ~520 nm.*[52]

Optical images of different parts of the patterned 2D perovskite (Figure 28a+c) are shown alongside their respective PL emission maps (b+d). It can be seen that the perovskite film follows the shape of the contacts underneath. Some areas in Figure 28b+c are higher in intensity, which might come from the deviations in film thickness and therefore could be generating more photons upon excitation. Some damage to the films can also be seen in both the optical image and the PL map. These are likely to be coming from the handling of the sample after the production process.

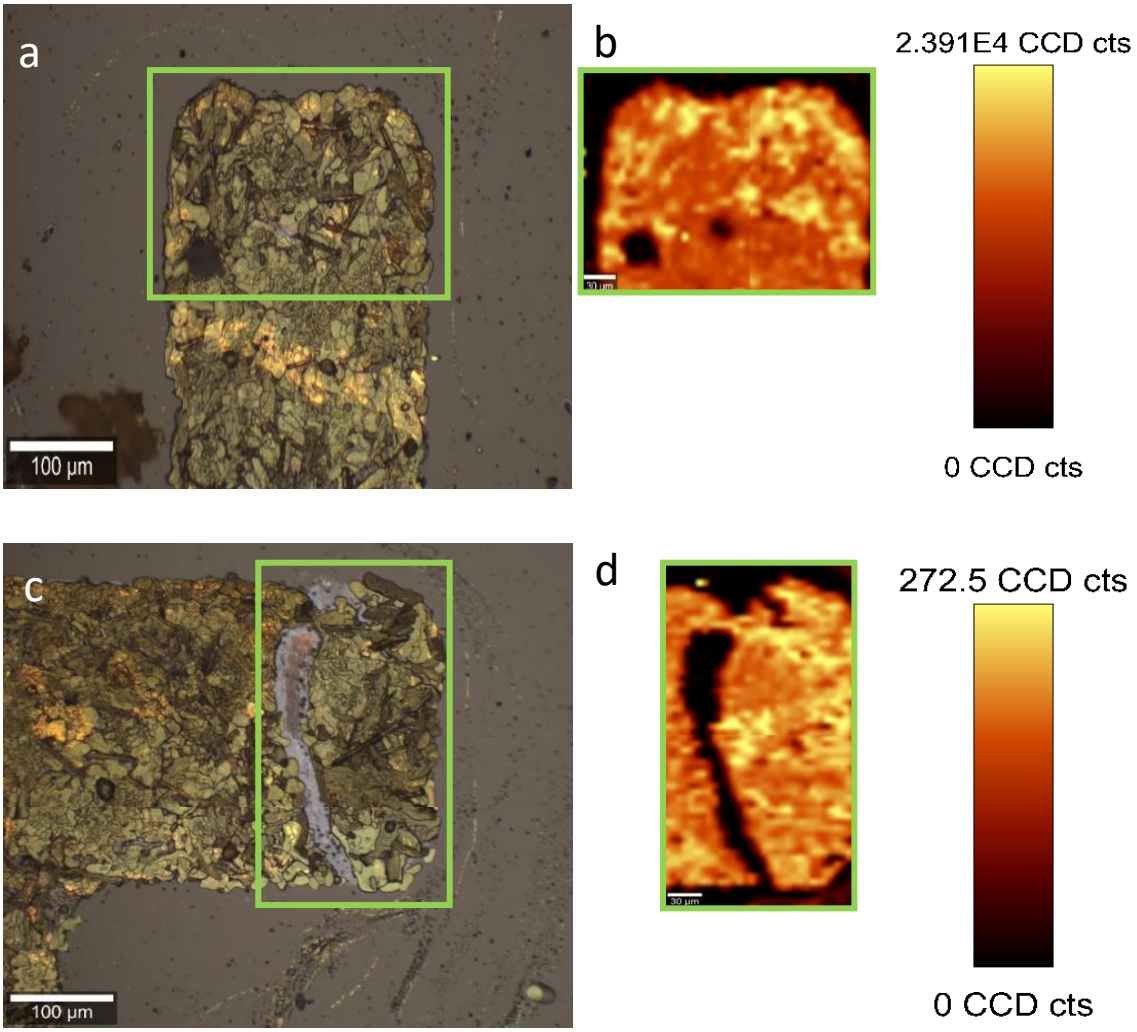

***Figure 28**: Optical image with a PL map of 2D perovskite on top of the patterned NiO_x/gold contact area. PL intensity is shown in the legends on the right side of the image. CCD counts were plotted for a wavelength of 525 nm.*

When thickness of the films was measured with a profilometer very large differences in thickness were found. The base of the measured areas of this IBC sample was close to 1.6 microns. However, spikes occurred to heights of 2 microns over a measured area of 400 microns in length. This could occur due to formation of other structures or due to the gaps in between the grain clusters. The average film thickness is shown in Table 2 and similar to the bulk samples this increased up to a factor 12 when compared to the thicknesses of the PbO_2 films.

Table 2: Thicknesses of PbO_2 films before and after conversion to 2D perovskite based on different electrodeposition times.

Deposition Time (s)	Film thickness after EC (nm)	Film Thickness after CVD (nm)
60	528	Not converted
30	268	Not measured
10	128	1590
5	73	600-900
3	35	500-700
2	18	450-600

Based on the optical, SEM, XRD, UV-VIS and PL data it has been shown that patterned PbO_2 films could be electrochemically deposited and subsequently converted into $(PEA)_2PbI_4$ with CVD. The 2D perovskite remained confined on the electrode areas and did not form on top of the quartz substrate. Therefore the final fabrication step in this research could be performed, the formation of the 2D/3D heterojunction.

3.4 2D/3D fabrication

In this section the fabrication and characterization of the 2D/3D heterojunction is discussed. This will be divided in three subsections based on the methods used. Firstly, spin-coating will be discussed, followed up by a so called 'stamping' technique which did not lead to a satisfactory result. Finally, the successful thermal evaporation of 3D perovskite will be elaborated upon.

3.4.1 Spincoating

***Figure 29**: optical image of spin-coated 2D/3D structure, circle highlights yellow spot on sample where no 3D perovskite had formed and underlying 2D layer was still visible.*

Spin-coating of a 3D perovskite layer on top of an existing 2D perovskite was explored as a first option to form the 2D/3D heterojunction. The spin-coating technique is well known for 3D perovskites and therefore relatively easy to reproduce. Usually when a 2D/3D heterojunction is formed by spin-coating a 2D layer on top of a 3D perovskite layer two different techniques are used.[23] An excess of PbI_2 for the 3D precursor can be used during spin-coating. After formation of the 3D perovskite film an organic spacer, dissolved in a suitable solvent such as isopropanol, is spin-coated on top of this film. The organic spacer can then react with the excess PbI_2 in the 3D perovskite film.[84] On the other hand a standard precursor solution for 2D and 3D perovskites can be used with subsequent spin-coating steps where the 2D perovskite is deposited on top of the existing 3D perovskite layer.[85] However, for formation of 3D perovskite on top of an already existing 2D perovskite layer this method was not straightforward. Two problems came up during this synthesis. The first problem involved the precursor

solution. The precursor solution that was used for the 3D perovskite consisted of a mixture of DMF and NMP as solvents. These liquids dissolved the 2D perovskite, which lead to both formation of quasi-2D perovskite structures during the crystallization phase and disappearance of the 2D perovskite. An optical image of a film resulting from this process is shown in Figure 29, which shows that a part of the 2D perovskite was not covered by 3D perovskite (encircled area). The rest of the film had a gradient of black and red colours. Outside of this area no 2D perovskite remained underneath this 3D layer as seen by observations of the black colour of the sample. To try and decrease the impact of this dissolution the method was adapted from a static to a dynamic spin-coating process. In this way the contact time between the solvents and the 2D perovskite was minimized. The second problem was the morphology of the $(PEA)_2PbI_4$ layer. The large height differences that were discussed in section 3.2 lead to problems, since some parts of the 2D perovskite where way thicker than others, due to this the 3D crystallization process was be influenced and therefore no homogeneous film could form. This was confirmed by the PL measurements, which did not show any emission of 2D perovskite outside of this one small yellow area. The PL emission maps (figure 30) show mostly 3D perovskite emission, but at certain locations on the sample a wavelength indicative of n=2 $(PEA)_2PbI_4$ (570 nm) could also be observed. This could be due to deposition of PEAI precursor during the CVD method. Besides the yellow area no n=1 emission of $(PEA)_2PbI_4$ could be observed, which indicates that the 2D perovskite dissolved during the spin-coating process. Therefore another technique was investigated.

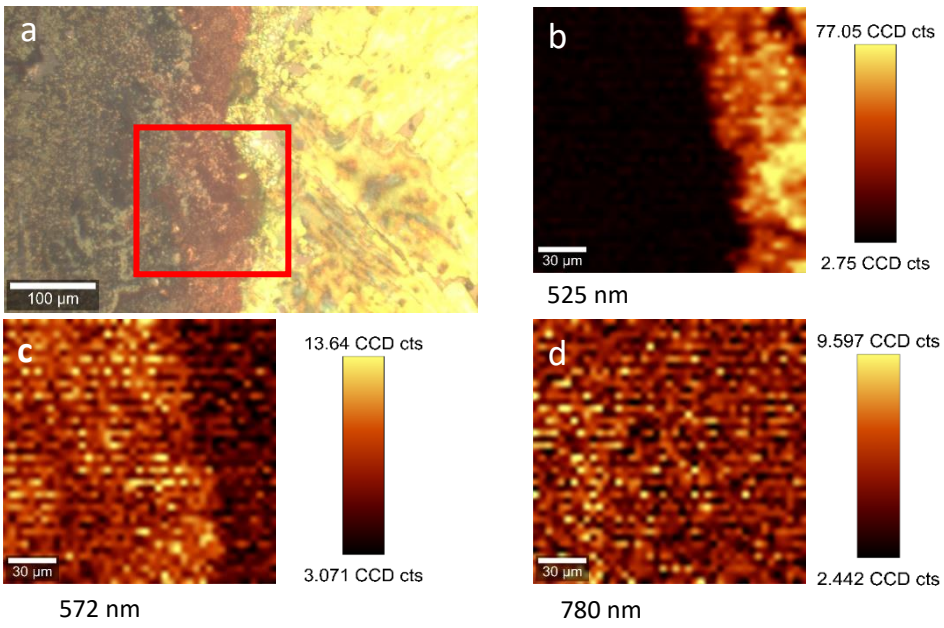

***Figure 30**: Optical image (a) of 3D perovskite spincoated on top of 2D perovskite. PL maps (b-d) of different wavelengths indicating n = 1 2D perovskite (b), n = 2 2D perovskite (c), and 3D perovskite (d) PL intensity is shown in the legends on the right side of the image.*

3.4.2. Stamping

The stamping method applied in this research was based on the previously mentioned solid in plane growth (SIG).[39] In SIG a 2D layer is spin-coated and subsequently (partially) transferred on top of an existing 3D perovskite film. Herein, this method was adapted to transfer a 3D perovskite on top of the existing $(PEA)_2PbI_4$ layer and will be referred to as stamping. Initially it was tested if a 3D perovskite was transferable between two different substrates. When the sample was annealed after spin-coating (such as in a regular perovskite spin-coating procedure) the film appeared to be non-transferable while applying heat and pressure. However, when a spin-coated film was stamped on top of a cleaned glass

substrate directly after the spin-coating (i.e. without annealing it first) the perovskite was partially transferred to said glass substrate (Figure 31e+f). A possible hypothesis for this difference could be that the perovskite structure is not fully formed before the annealing step, therefore some perovskite could still be dissolved in remaining solvent. By evaporation of these solvents due to the applied heat and pressure recrystallization could be induced. This might also be a reason for the partial transfer of the film. Another possible reason for the partial transfer could be that the pressure wasn't distributed evenly across the sample. However, this transfer mechanism wasn't investigated in further detail. When it was shown that this method could work it was applied to the 2D perovskite samples.

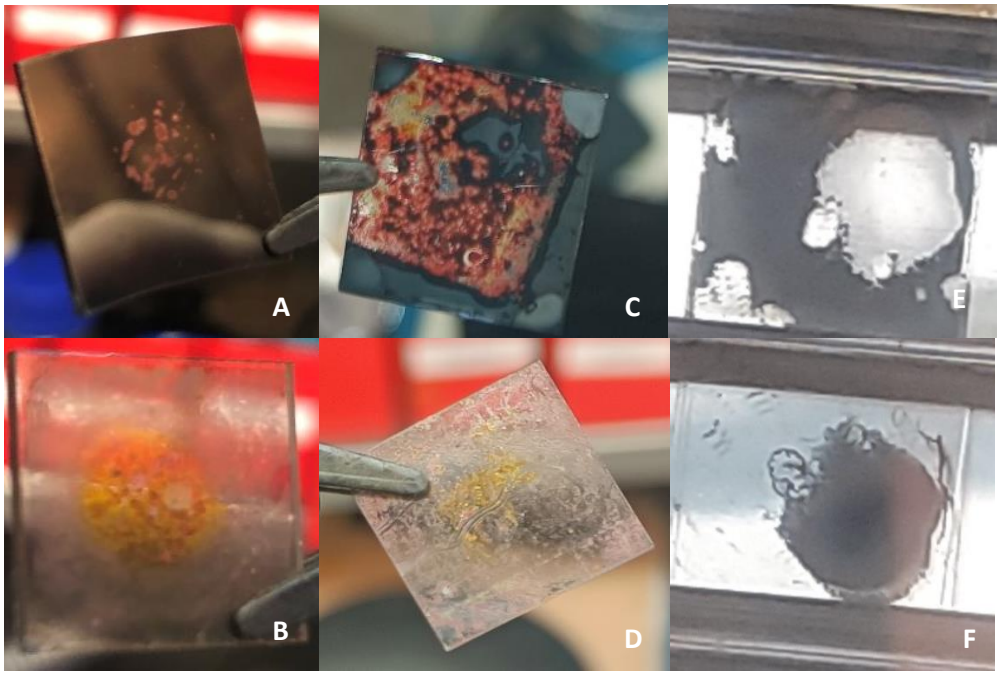

Figure 31: *Stamped perovskite films with pre-annealing of 3D film before stamping (a+b), 3D stamp (a), 2D perovskite after stamping (b). Stamped perovskite films without pre-annealing the 3D film before stamping (c+d). Stamped 3D perovskite on clean glass substrate (e+f)*

The two different methods for stamping described above where used in the fabrication of the 2D/3D heterojunction. As shown in Figure 31a+b the 3D film that was annealed for 10 minutes before stamping only showed transfer of some 2D material onto the 3D film. However when stamping took place directly after spin coating more of the 2D film got transferred, and almost none remained on the previous substrate (Figure 31c+d). As shown in the PL maps of Figure 32, the stamped areas show emission centered at wavelengths of 525, 572 and 780 nm. This indicates that besides the n=1 (525 nm) and 3D perovskite (780 nm), also n=2 2D perovskite (572 nm) is present on the sample. With both methods mostly the 2D perovskite is transferred towards the 3D and not the other way around. Due to morpholigical differences in the 2D samples (as shown in section 3.2) not all areas of the 3D perovskite came into contact with the 2D perovskite films. Therefore only some areas are transferred. The fact that the 3D perovskite sample without pre-annealing shows more transfer and more formation of n=2 perovskite could possibly come from the remaining solvent dissolving the 2D perovskite or the excess PEAI precursor left from CVD. Why no emmission wavelengths of higher dimensional 2D perovskite (n>2) were observed in the PL measurements is unclear.

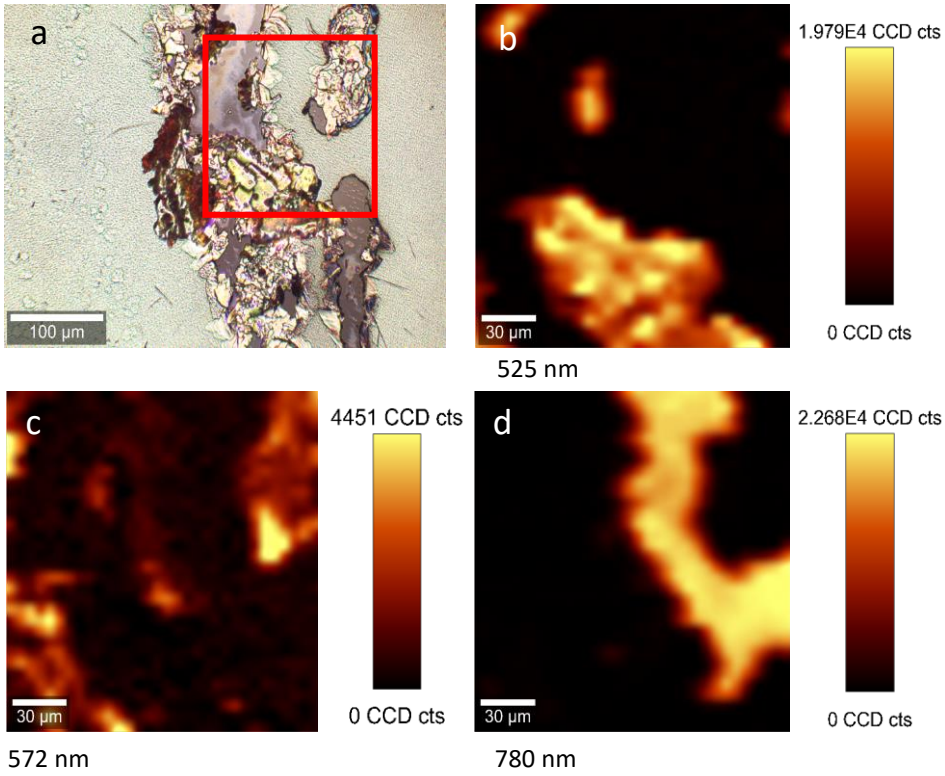

***Figure 32**: Optical image (a) Of 3D perovskite film with 2D perovskite on top (after attempt to stamp 3D perovskite on top of 2D perovskite). PL maps (b-d) of different wavelengths indicating n = 1 2D perovskite (b), n = 2 2D perovskite (c), and 3D perovskite (d) PL intensity is shown in the legends on the right side of the image.*

3.5 Thermal evaporation:

Since it has been shown that neither the spin-coating nor the stamping techniques formed the desired 2D/3D heterojunction another technique was investigated: thermal evaporation of a thin 3D perovskite layer on top of the existing 2D perovskite. For this step samples were sent to the University of Cambridge. During their process the 3D perovskite is usually annealed for prolonged time at 135 °C in order to get the correct crystal structure of $FA_{0.7}Cs_{0.3}Pb(I_{0.9}Br_{0.1})_3$.[86] However, due to the $(PEA)_2PbI_4$ layer this annealing step was put on hold. Annealing the sample might result in changes in the dimensionality of the 2D perovskite material, or it might induce degradation of the material. Four different kind of samples were created; two reference 3D samples (i.e. one on NiO_x/ITO and the other on quartz with the patterned NiO_x/Au contacts). One 2D/3D sample on NiO_x/ITO and one 2D/3D sample on quartz with the patterned NiO_x/Au contacts.

3.5.1 3D reference sample on NiO_x/ITO:

Visually the deposited 3D perovskite layer looked yellow, which could be caused by the low film thickness (~50 nm). The peaks at 14.0 and 28.0 indicate the formation of 3D perovskite (Figure 33).

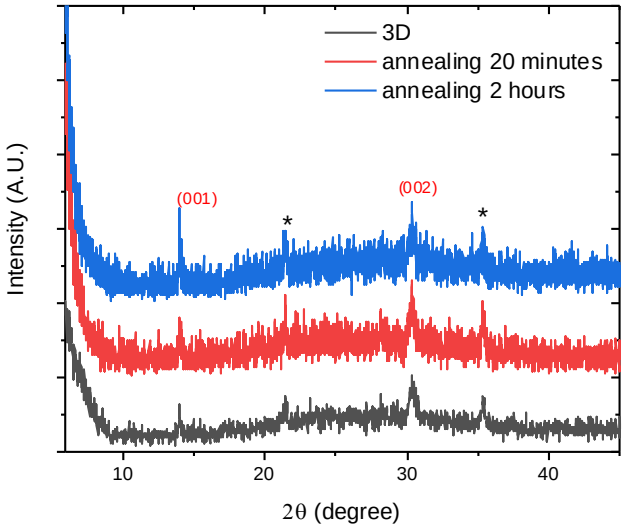

***Figure 33**: XRD graphs of as deposited 3D perovskite before and after annealing.*

However, in the PL emission spectra the expected peak emission wavelength of 770 nm was not observed immediately after excitation with the 405 nm laser. Instead, a broad emission wavelength was observed between 520-640 nm (Figure 34)**.** During prolonged excitation with the 405 nm laser a red shift of the peak was observed towards ~750 nm together with an increase in intensity. Due to this peak shift during laser excitation it was believed that the laser locally annealed the sample to form the correct crystal structure of the 3D perovskite. Therefore the sample was annealed on a hot plate for 2 hours at 100 °C to form this conformation. After the annealing the sample changed from yellow to light brown. In Figure 34c the time series of the perovskite film after annealing is shown. The emission initially goes down, but in the final 50 seconds of the measurement it remained stable. The emission wavelength shifted to the expected value after annealing. The change in intensity is caused by the different laser intensities used in the measurements. Before annealing a higher laser power was used and therefore the intensity decreased after annealing.

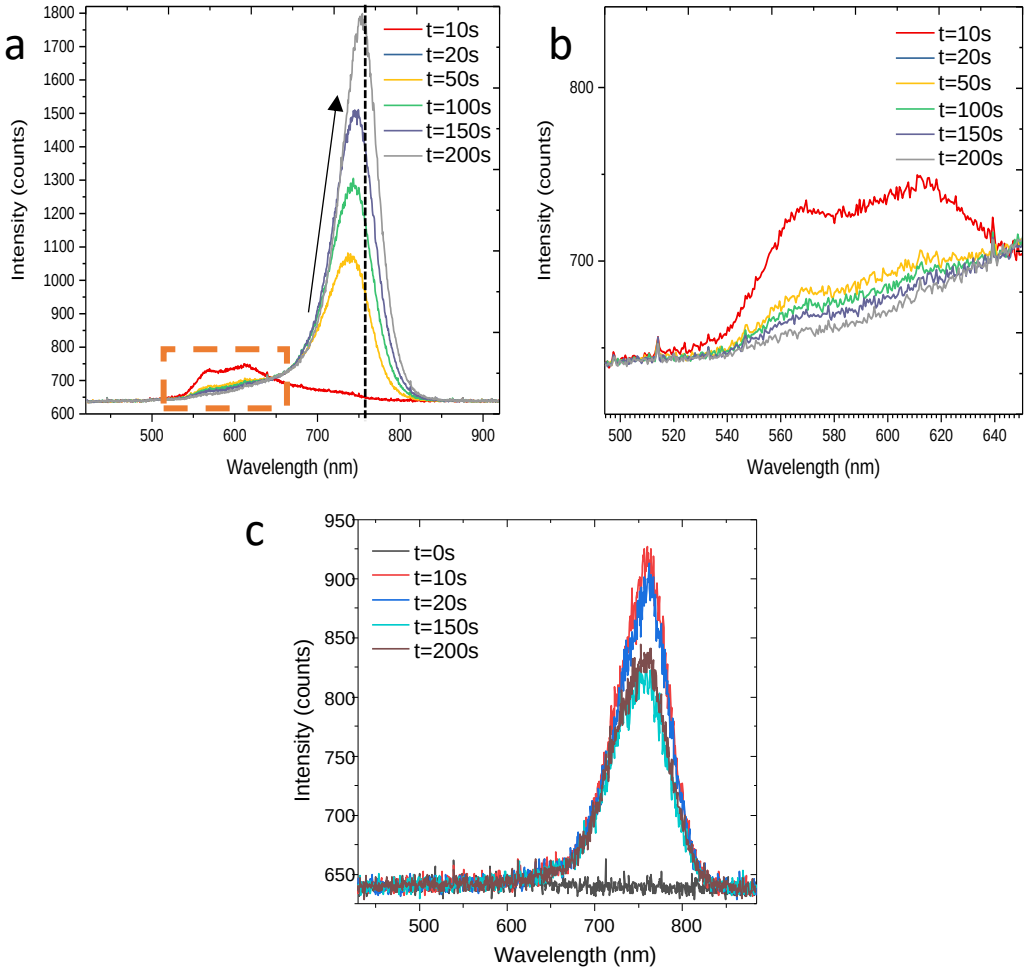

Figure 34: *PL emission time series of evaporated 3D perovskite film on top of NiO_x/ITO (a), zoom of highlighted area in a (b) and time series after annealing for 2h at 135 C (c).*

3.5.2 2D/3D samples on NiO_x/ITO

For the bulk samples the PL emission spectra the expected peak of 770 nm was also not observed immediately after excitation with the 405 nm laser. During prolonged excitation with the 405 nm laser a red shift of the peak was observed towards ~750 nm together with an increase in intensity. It was suggested to anneal the 2D/3D samples at 90 °C for 20 minutes, since this annealing temperature was regularly used by Dr. Borchert after evaporation of 2D perovskites. It was expected that this would induce the least changes in the 2D perovskite layer. After annealing the colour of the sample changed from yellow to red, which would indicate a transition from *n*=1 to *n*=2. In Figure 35 the peaks at 5.5, 11.0 and its repetitions show the presence of the $(PEA)_2PbI_4$ and the peaks at 14 and 28 indicate the presence of the 3D perovskite layer. The *n*=2 perovskite peaks were not seen in the XRD, it is unclear why not.

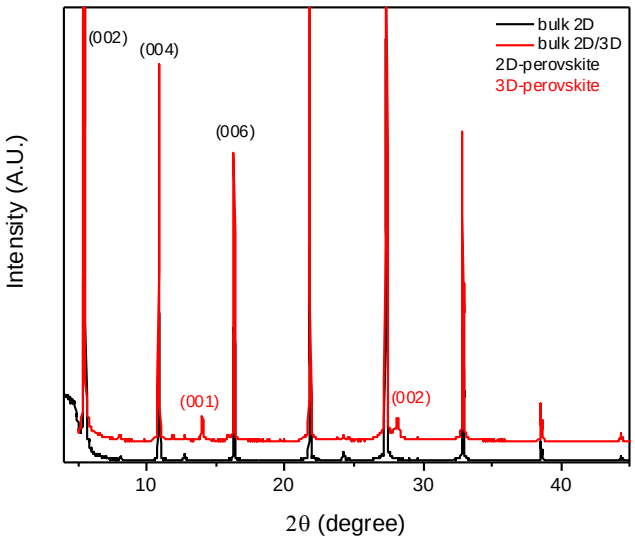

***Figure 35**: XRD graph of bulk sample before (black) and after deposition of 3D layer (red).*

During PL measurements three distinct peaks were observed at 520 nm, 575 nm and 745 nm (Figure 36). These wavelengths correspond with *n*=1, *n*=2 $(PEA)_2PbI_4$ and 3D perovskite respectively. The peak at 575 nm of the *n*=2 perovskite can explain the colour change from yellow to red. Furthermore, some areas showed red colour, implying the presence of *n*=2 2D perovskite, even though no 2D perovskite was deposited in that area. This could come from PEAI deposited during CVD, that came into contact with the 3D perovskite and then formed some quasi 2D structure. During the PL time series the emission wavelength of the 3D perovskite blue-shifted and peak intensity increased over time. In contrast the *n*=1 and *n*=2 peaks decreased in intensity. This could possibly be indicative of energy transfer from the 2D layer to the 3D layer.[87]

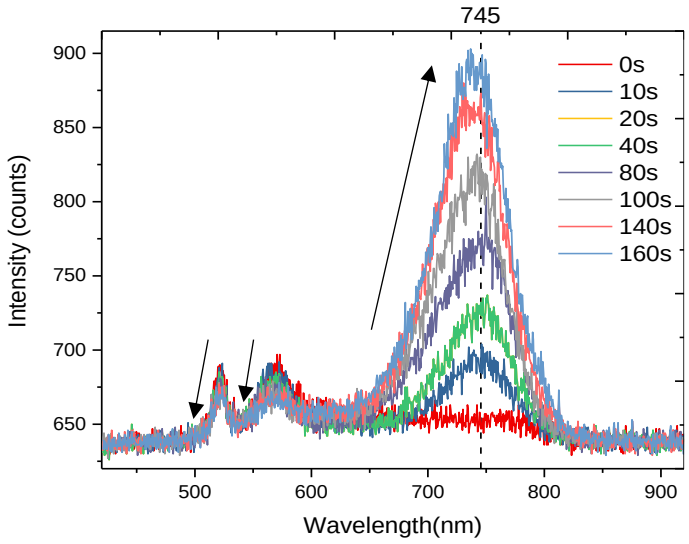

***Figure 36**: PL emission time series of 2D/3D perovskite on NiO_x/ITO substrate.*

3.5.3 Reference 3D perovskite on IBC samples

The IBC samples showed the same yellow colour across the 3D layer. Similar to the 3D bulk sample, the IBC reference 3D sample showed signs of annealing during laser excitation. In Figure 37 it is shown that the PL emission of the 3D perovskite on top of the contacts and on top of the quartz substrate differ significantly, the wavelength on the contacts is centred around 700 and 740 nm, while on top of the glass substrate the wavelength is centred around 600 nm and the intensity is an order of magnitude smaller. This indicates that the 3D perovskite has formed differently on different substrates. Although neither of these higher wavelengths are the expected wavelength of the 3D perovskite, which should be centered around 770 nm.

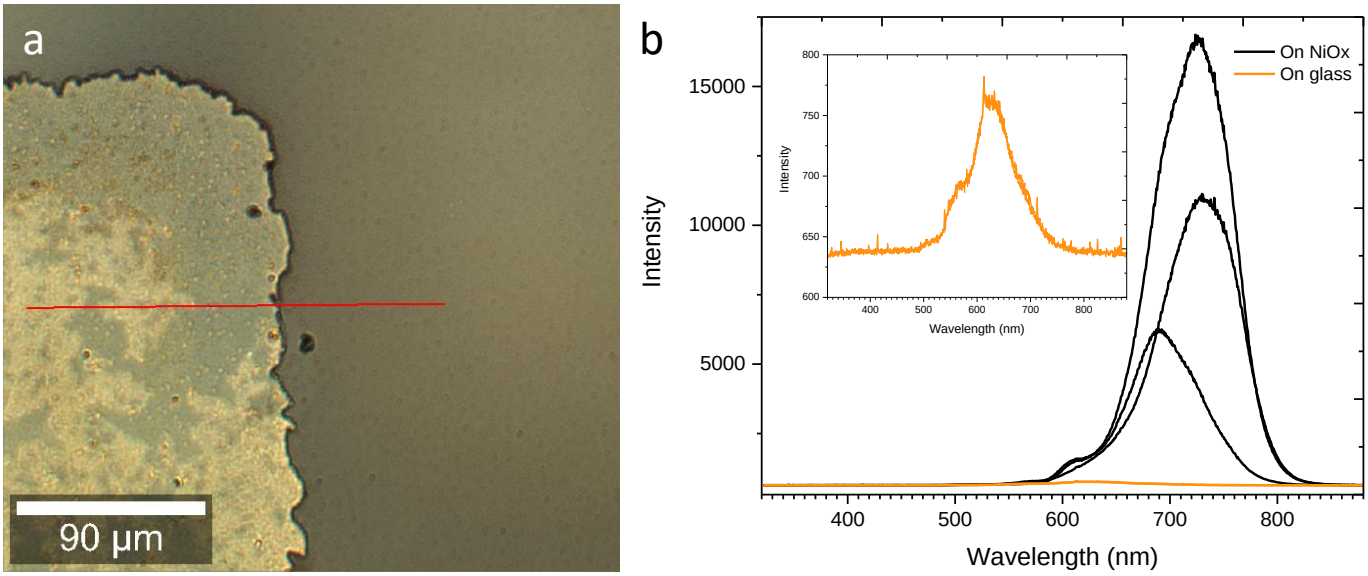

***Figure 37**: Optical image of 3D perovskite on IBC sample (a) and PL linescan across the contact and quartz substrate (b).*

3.5.4 2D/3D perovskite on top of NiO_x/Au patterned contacts.

Evaporation of 3D perovskite on top of the patterned 2D perovskite devices lead to a 2D perovskite layer that was still clearly visible by eye and was contained on the NiO_x/Au contacts. The yellow 3D perovskite could be seen both on top and next to the contacts, optical microscopy images supported these observations (Figure 38).

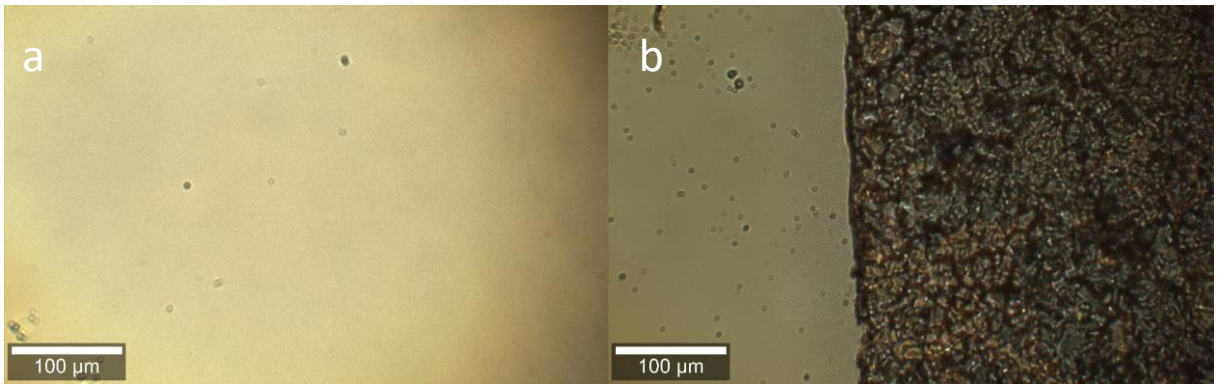

***Figure 38:** Optical images of IBC sample with 3D perovskite on glass (a) and on top of 2D perovskite layer on Au/NiO_x contacts (b).*

Similar to the bulk 2D/3D samples, the XRD graphs (Figure 39) showed peaks of both 2D and 3D perovskite layers. A gold peak at 38 2θ was also observed here. Additionally a small PbI_2 peak was seen at 12.7 2θ, both before and after annealing.

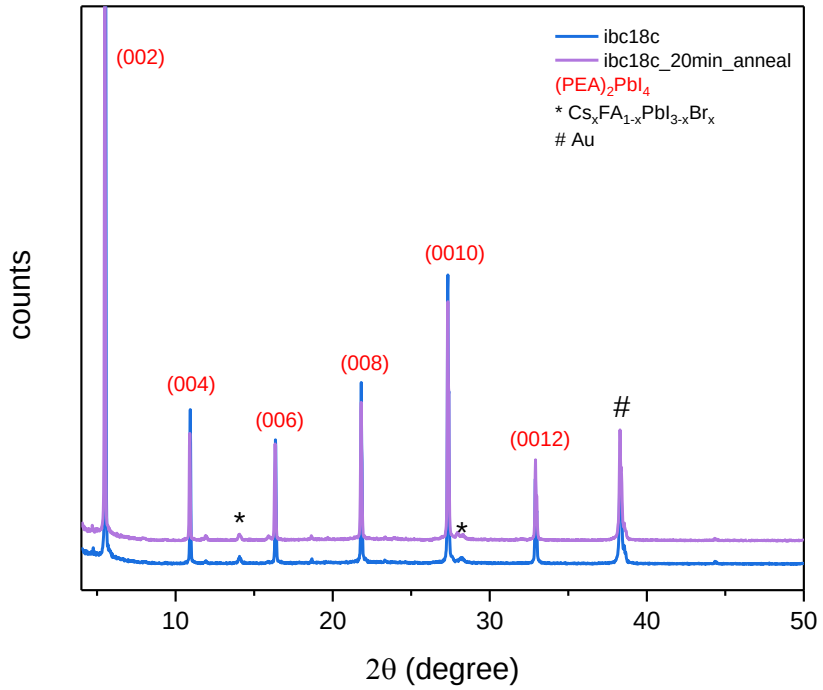

Figure 39: *XRD graph of 2D/3D heterojunction on quartz substrate with NiO_x/Au contacts.*

Additionally, when looking at the PL spectrum a similar trend to the bulk 2D/3D sample was observed. Before annealing, the 3D perovskite layer showed contributions from two different broad peaks, one located at 580 nm and the other around 700 nm. During a time series this first peak shifted towards 605 nm and the second peak shifted towards 745 nm (Figure 40a). On the 2D deposition area (on top of the NiO_x/Au contact) A sharp peak at 520 nm was observed as well as a broad peak centred around 700 nm which shifted towards 770 nm during laser excitation. In a time series measured on top of the contact (Figure 40c) it was shown that the peaks at 520 nm and 700 nm went down in intensity over time, while a new peak at 575 nm formed and the peak at 770 nm began to grow in intensity over time. Therefore it was assumed that these shifts could be attributed to film annealing during laser excitation, as was seen before for the other films as well. The same annealing time and temperature as for the 2D/3D bulk sample was used (20 min, 90 °C). In another time series (Figure 40d) the sample showed similar behaviour as before annealing although the peak at 770 nm could be observed from the start of the time series measurements. The peak at 770 nm that showed from the start of the time series indicated that 3D perovskite did form and the shift of the intensities come from funnelling of emission from the higher to the lower bandgap material (i.e. the 3D perovskite). The formation of a peak at 575 nm indicated once more that n=2 $(PEA)_2PbI_4$ had formed during the annealing. This might come from thermally induced intercalation of PEA^+ into the 3D perovskite film.

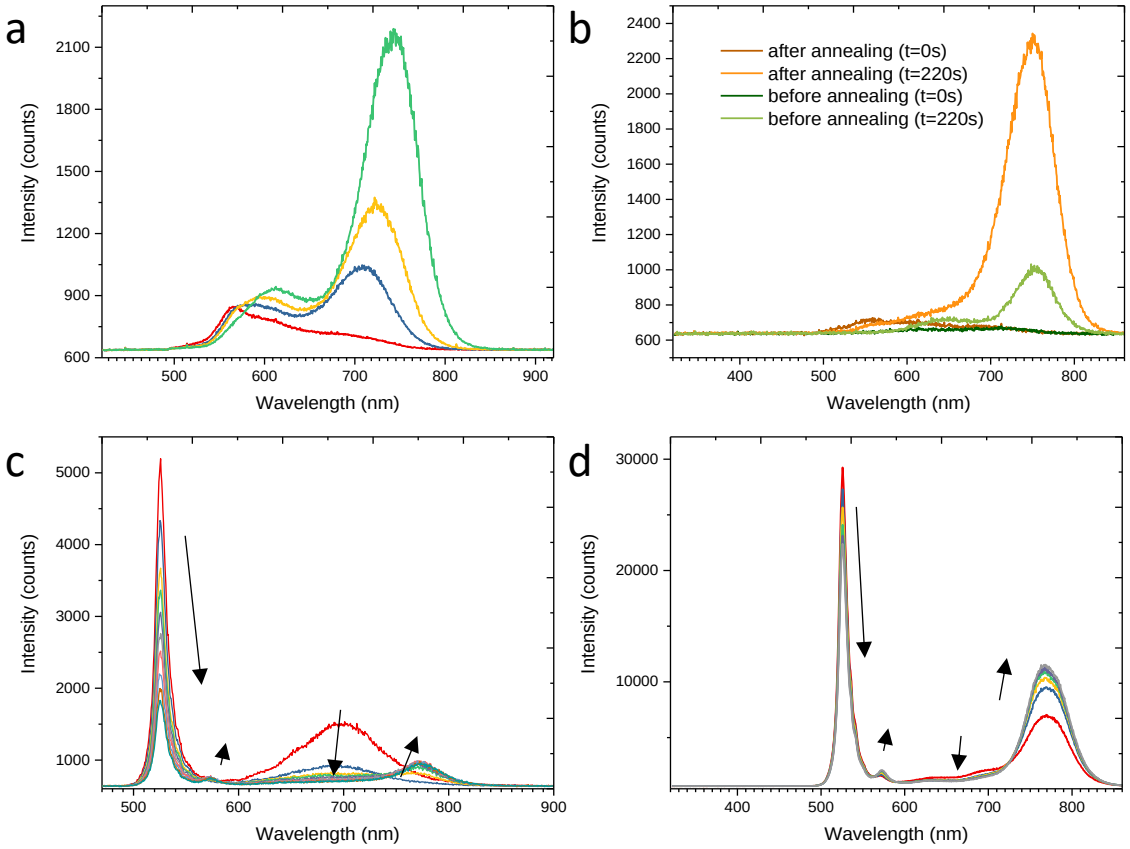

Figure 40: *time series 3D perovskite on quartz (a), before and after annealing (b), time series on top of 2D/NiO_x/Au contact area before (c) and after annealing (d).*

3.6 Transient PL on 2D/3D heterojunctions

The 2D/3D heterojunctions were used to measure transient photoluminescence (TRPL). First an evaporated 3D sample was measured in two different spots to find the reference decay time. Then a 2D/3D bulk structure was measured at three different spots, two on top of the heterojunction and one were only 3D material is present (Figure 41). To compare the two different measurements only the photoluminescence of the 3D perovskite should be captured by the CCD, therefore a 650 nm longpass filter was used to filter out any emission from the 2D perovskite.

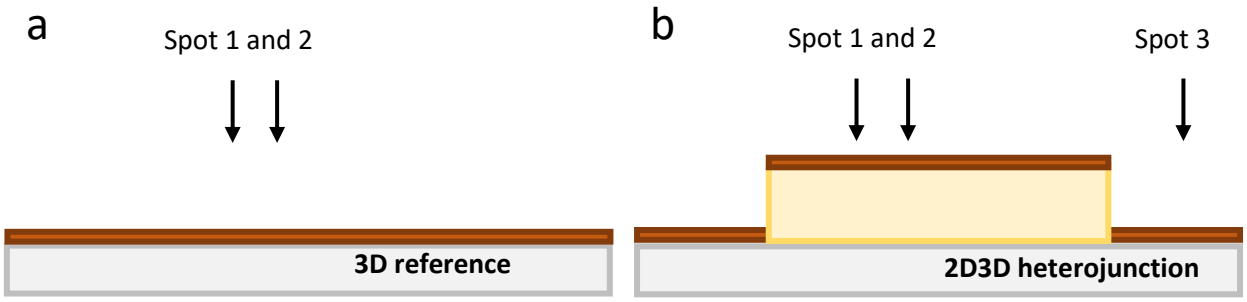

Figure 41*: illustration of the different TRPL measurement locations of the samples*

The TRPL maps (Figure 42a-d) show the different locations of the samples that have been measured. For the original decay curves the fitted background values were subtracted and subsequently the decay trace was divided over the maximum value of the decay trace. The fits are made by fitting the raw data and then normalizing with the same maximum value of the raw data traces. Therefore the fits do not start exactly at 1.00. This fit was performed with a double exponential function (eq. 11), where *i* is 2, t_0 is the start time of the fit (which is not necessarily 0 during the measurement), A[i], t[i] and $Bkgr_{Dec}$ are fitted parameters.

$$y(t) = \sum_{i=0}^{n-1} A[i] \exp\left(-\frac{t - t_0}{\tau[i]}\right) + Bkgr_{Dec} \qquad [11]$$

The fitted decay traces from these maps are shown in Figure 42e, and the coefficients for each fit are shown in Figure 42f. Here it can be seen that the PL lifetime increased for spot 1 and 2 of the 2D/3D heterojunction when compared to the 3D reference sample. From this it is implied that this increase in lifetime might come from passivation of the 3D perovskite layer by the 2D perovskite underneath, or from the increased amount of charge carrier from absorption of the 2D perovskite layer and subsequent transfer of these charge carriers to the lower bandgap 3D perovskite layer.[35] The 3D perovskite has a limited thickness of 50 nm and the general penetration depth of a 405 nm laser is higher than that.[35,88] The third spot of the heterojunction showed lower lifetimes, which could indicate that 3D perovskite alone is less passivated, however it is not clear if the composition of the material at that spot was pure 3D perovskite or a mix of PEAI material with 3D perovskite materials. To check if charge carrier transfer occurs, TRPL measurements with a laser below the bandgap of the 2D and above the bandgap of the 3D (i.e. λ = 640 nm) perovskite could be performed. With this laser the 3D perovskite can be excited selectively, therefore excluding the possibility of charge carrier generation in the 2D perovskite and subsequent transfer to the 3D perovskite.

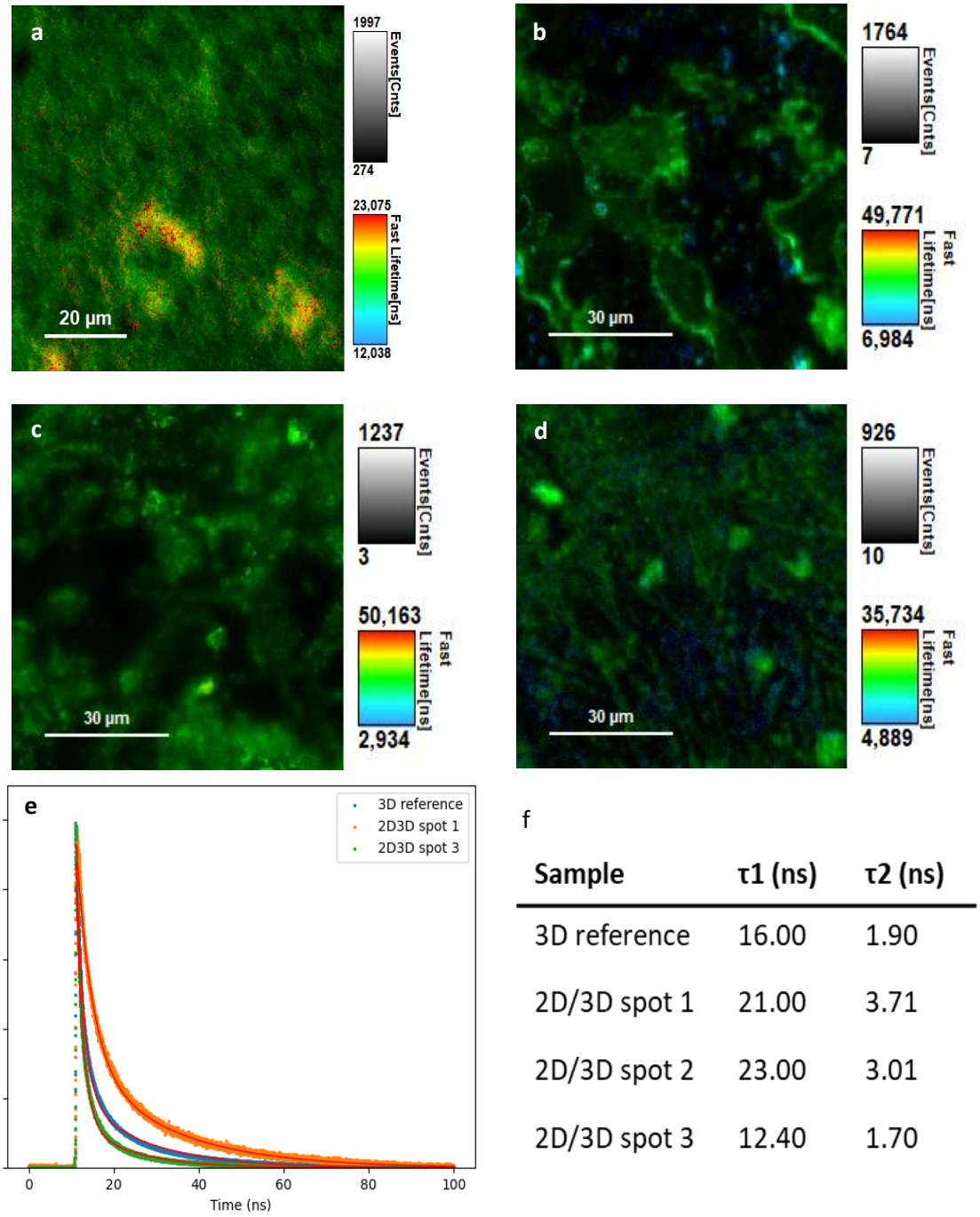

Sample	τ1 (ns)	τ2 (ns)
3D reference	16.00	1.90
2D/3D spot 1	21.00	3.71
2D/3D spot 2	23.00	3.01
2D/3D spot 3	12.40	1.70

***Figure 42**: TRPL data. Emission maps of (a) 3D reference, (b) 2D3D heterojunction spot 1, (c) 2D3D heterojunction spot 2, and (d) 2D3D heterojunction spot 3. These maps were all made with a 650 nm longpass filter. (e) Normalized TRPL decay traces and fitted data. (f) lifetimes of the function of eq. 11*

In this section it has been shown that a 2D/3D heterojunction was made by evaporation of the 3D perovskite layer on top of the 2D perovskite. Despite difficulties with creating a clear 2D/3D heterojunction without formation of *n*>1 phases, one of these samples showed indication of increased PL lifetimes when compared to a reference 3D perovskite sample.

4. Conclusion and Future Outlook

In this research two main aims were formulated. First it was investigated if a 2D/3D heterostructure can be formed and characterised on an IBC patterned substrate. As a proof of concept PbO_2 could be deposited electrochemically on top of a NiO_x/ITO substrate. Subsequently these PbO_2 films could be converted into $(PEA)_2PbI_4$ with CVD. Based on the data it was shown that this conversion could take place, albeit in two steps with PbI_2 formation sometimes and low control over the morphology. Afterwards a 2D/3D heterojunction was formed. Whilst solvent based methods showed that the 2D layer would dissolve and the solid in-plane growth method did not transfer enough material from one substrate to the other. In the end it has been shown that a 2D/3D heterojunction was made by evaporation of the 3D perovskite layer on top of the 2D perovskite. Therefore the knowledge from the bulk samples could be transferred to the patterned substrates. The 2D perovskite remained confined on the electrode areas and did not form on top of the quartz substrate. Subsequently the 3D perovskite could be evaporated on top. Although, this required annealing of the sample which altered the 2D/3D heterojunction to form an *n*=2 layer. The second aim was to investigate what influence this 2D perovskite interlayer had on the charge carrier dynamics of the 3D perovskite. With TRPL these samples indicated increased PL lifetimes when compared to a reference 3D perovskite sample. Although it remains unclear whether this is due to passivation.

It would be interesting to do more studies into the role of this 2D perovskite layer as passivation layer, a way this could be done is to look at the morphology of the 2D perovskite with different techniques such as AFM. Additionally, optimizing the thickness of the 2D perovskite interlayer would be interesting to see if an actual interlayer could be made instead of a very thick 2D perovskite layer that acts more as a barrier for charge transfer and extraction than as a passivation layer. A second way to study the role of the 2D perovskite as a passivation layer would be to make an IBC substrate with a more intricate pattern with less space between the two contacts. Therefore it would be possible to do conductivity studies. Besides looking at passivating effects making perovskites on these intricate patterns could also be a way to investigate other properties, such as the ability to grow the perovskites in a vertical orientation instead of horizontal layers. Another way for that would be making an asymmetric device i.e. changing one of the two electrodes to contain an electron transport layer instead of an hole transport layer like nickel oxide. Finally, different organic spacer cations could be introduced instead of phenethyl ammonium that includes a heteroatom besides nitrogen (e.g. sulphur or fluorine). In this way, when cross-sectional SEM is performed on a 2D/3D device energy-dispersive x-ray spectroscopy could also be performed to characterize the two different layers. This could help when a very small interlayer is formed. Furthermore, it would be interesting to study the charge transfer effects in more detail. As mentioned before in section 3.6 TRPL measurements with a laser below the bandgap of the 2D perovskite and above the bandgap of the 3D perovskite could be performed (i.e. λ = 640 nm). With this laser the 3D perovskite can be excited selectively, therefore excluding the possibility of charge carrier generation and transfer in the 2D perovskite.

These future studies give an opportunity to gain more insights in the 2D perovskite as a passivation layer. Additionally, patterning of perovskite layers through the combination of electrodeposition and vapour deposition could be of great use for other studies when the control over thickness and morphology is optimized.

5. Acknowledgements

First of all, I would like to thank prof. Bruno Ehrler and dr. Esther Alarcon Llado for the opportunity to do this shared project in both of their groups. Secondly, I would like to thank Imme Schuringa and Daphne Anthony for the shared supervision during this project. Both of you thought me different expertise and skills during this project and it was wonderful working with you. Working in two different research groups at the same time can bring a lot of both positive and negative things but I've mostly experienced the positive effects due to the both of you! I would also like to thank prof. Joost Reek for being the second examiner for my thesis.

Furthermore, I would like to thank the rest of the group members of the Hybrid Solar Cells and 3D photovoltaics groups for their discussions during meetings, nice lunches, coffee breaks and general fun times. Especially during the HSC group trip in November 2021. Special shout-out to Yorick Bleiji who was always cheerful and ready to help me when I ran into yet another problem with the electrochemical setup.

Together with both of these groups and all the other amazing people at AMOLF this internship has been a delight and a great opportunity to learn. Thank you all!

6. Experimental

Sample fabrication

Preparation of NiO_x/TCO substrate

A 15 mm x 15 mm piece of tin-doped indium oxide (ITO) on glass was used as a base substrate (unless mentioned otherwise). These were cleaned with a brush and detergent and sequentially ultra-sonicated in demineralized water, acetone, isopropanol and dried with nitrogen and then cleaned by UV/ozone for 30 minutes before use. A 7 nm Ni layer was deposited by electron beam physical vapor deposition. This Ni layer was subsequently annealed to NiO_x in two heating steps. In the first step the substrate was heated to a temperature of 250 ℃ with a ramp of 10 ℃/min and kept there for 30 minutes. In the second step the temperature was increased to 300 ℃ with a ramp of 5 ℃/min and kept there for 5 minutes

Electrodeposition of PbO_2 films on NiO_x/ITO

$Pb(NO_3)_2$ powder (1.655 g, 5 mmol) was weighed and transferred to a beaker. Subsequently water (50 mL) was added. The aqueous $Pb(NO_3)_2$ solution (0.1 M) was transferred to an NaOH solution (0.1M) to increase the pH. All solutions were prepared in water from a Millipore Milli-Q system. Electrodeposition was performed without stirring at ambient temperature with a Biologic SP-300 potentiostat and a three-electrode arrangement. 15 mm x 15 mm NiO_x/ITO glass substrates were ozone cleaned for 20 minutes and used as the working electrode. The circular active deposition area being ~0.38 cm^2. A circular platinum mesh was used as the counter electrode and an eDAQ ET072 Ag/AgCl electrode as the reference electrode. The deposition time ranged from 1 to 120 s. After the deposition, the PbO_2 films were rinsed with Milli-Q water and dried with nitrogen. Depositions were done potentiostatically at a potential of 1.5 V unless stated otherwise.

Preparation patterned contacts

14 mm x 16 mm pieces of quartz were used as substrates. These substrates were cleaned in the same way as the ITO substrates (see Preparation of NiO_x/TCO substrate). A shadow mask with interdigitated patterns was used for the deposition of the conducting metals. Sequentially 5 nm Ti, 30 nm Au and 7 nm Ni were deposited by electron beam physical vapor deposition. The Ni layer was annealed with the same heating profile as used for the Ni/ITO substrate. Electrodeposition of PbO_2 films on NiO_x/Au contacts followed the same procedure as the electrodeposition of PbO_2 films on NiO_x/ITO (see Electrodeposition of PbO2 films on NiOx/ITO). The active deposition area was 13.4 mm^2 and the deposition times ranged from 1 to 60 s.

Conversion of PbO_2 to $(PEA)_2PbI_4$ (Chemical Vapor Deposition)

The PbO_2 substrate was placed into a vacuum tube furnace and a ceramic crucible with PEAI powder was placed on the left of the PbO_2 substrate. The tube furnace was purged with Ar or N_2 and subsequentially brought down to a pressure between 60 and 80 mbar with an Ar or N_2 flow of 30-35 mL/min. Subsequently the furnace was heated to temperatures ranging between 160 °C to 180 °C for 2 to 24 hours with a two-step heating program to 100 °C with 10 °C/min and to the desired temperature with 5 °C/min. After cooling the samples were stored in a N_2 environment.

Precursor solution preparation

A typical 3D perovskite precursor solution of $Cs_{0.18}FA_{0.82}PbI_{2.82}Br_{0.18}$ was prepared in a 9:1 DMF:NMP solvent mixture. For preparation of this solution PbI_2 (0.662 g), formamidinium iodide (0.189 g), and cesium bromide (0.052 g) were dissolved in DMF (0.9 mL) and NMP (0.1 mL). This solution was stirred

overnight to yield a 1.1M precursor solution. Right before spin-coating the precursor solution was heated to 100 °C for 15 minutes and allowed to cool down to room temperature.

Spin-coating of 3D on top of 2D:

65 µL precursor of $Cs_{0.18}FA_{0.82}PbI_{2.82}Br_{0.18}$ was spin-coated dynamically on ITO/glass substrate containing a layer of $(PEA)_2PbI_4$ for a total time of 40 s. The first step is 2000 rpm for 10 s with a 200 rpm/s ramp, followed up by a step of 5000 rpm for 30 s with a 2000 rpm/s ramp. After 2 s from the start the 65 µL precursor is poured on the substrate. After 15 s from the beginning an N_2 gun is used for quenching of the perovskite for 15 s with 5 bars pressure at 4-8 cm vertical distance from the substrate. Afterwards, the sample is immediately placed on the hot-plate at 100 °C for 10 min.

Spin-coating of 3D before stamping:

65 µL of $Cs_{0.18}FA_{0.82}PbI_{2.82}Br_{0.18}$ precursor was spin-coated statically on glass substrate with two steps for a total time of 40 s. The first step is 2000 rpm for 10 s with a 200 rpm/s ramp, followed up by a step of 5000 rpm for 30 s with a 2000 rpm/s ramp. After 15 s from the beginning the N_2 gun is used for quenching of perovskite for 15 s with 5 bars pressure at 4-8 cm vertical distance from the substrate. Afterwards, the sample is immediately placed on the hot-plate at 100 °C for 10 min, unless mentioned otherwise.

Stamping:

After spin-coating the 3D perovskite on a glass substrate the sample was placed on top of a $(PEA)_2PbI_4$ sample. On top of these two samples another glass substrate was placed to prevent breaking. This sample stack was placed underneath a press for 12 hours whilst heating to 100 °C. The samples were taken apart afterwards and investigated for transfer of perovskite material.

Evaporation:

3D perovskite deposition was performed by Dr. Juliane Borchert at the University of Cambridge, England, according to a previously published procedure.[86] This perovskite consists of a double halide and double cation composition of $FA_{0.7}Cs_{0.3}Pb(I_{0.9}Br_{0.1})_3$.

Characterization:

For the cyclic voltammetry measurement a Biologic SP-300 potentiostat and a three-electrode arrangement were used. 15 mm x 15 mm NiO_x/ITO glass substrates were ozone cleaned for 20 minutes and used as the working electrode. The circular active area being ~0.38 cm^2. A circular platinum mesh was used as the counter electrode and an eDAQ ET072 Ag/AgCl electrode as the reference electrode. The scan rate was 100 mV/s and ran from -2V to +2V vs Ag/AgCl.

X-ray diffraction (XRD) patterns of PbO_2, PbI_2, PEA_2PbI_4 were recorded/obtained using a Bruker D2 Phaser. The setup uses a Cu K_α tube to generate X-rays under variable angle θ (radiation wavelength = 1.5418 Angstrom). The increment used was 0.02 θ per step with time-steps of 0.1 s in a continuous PSD scan mode. Peaks at specific positions were characteristic for crystallisation properties of the film.

UV-Vis measurements were performed to obtain steady-state absorption spectra using a Perkin Elmer LAMBDA 750 spectrophotometer. The spectrophotometer is equipped with a photomultiplier tube (PMT) and an InGaAs detector an integrating sphere a deuterium lamp and a tungsten lamp, therefore allowing for a wide range of excitation wavelengths. The excitation wavelengths were measured between 250 and 860 nm.

Scanning electron microscopy was performed to analyse surface morphology and film thickness with a FEI Verios XHR SEM with nm resolution. Thickness was measured by cleaving samples in half to make cross-sections. Samples were mounted on a stub at a 45 ° angle and were tilted another 45 ° to make cross-sectional images. SEM was operated with a voltage of 5-10 kV and a current of 100 pA unless mentioned otherwise

Profilometer measurements were performed with a KLA Tencor Stylus Profiler P7 to analyse layer thickness. Deposited PbO_2 films and converted PEA_2PbI_4 films were scratched with sharp tweezers. A calibrated needle then moved along the film surface and measured the height difference next to and on the scratched area. Applied scan speed ranged from 20 – 50 µm/s and the applied force ranged from 0.5 to 2 mg.

Steady-state photoluminescence measurements were performed WITec alpha300 RS confocal imaging microscope system with a 20x magnification, air objective (Zeiss EC Epiplan 9903). The samples were excited with a continuous-wave laser of with a wavelength of 405 nm (Thorlabs S1FC405). The reflection was collected in reflection mode with a WITec UHTS spectrometer with a 600 g/mm grating. The laser light was filtered out during measurements with a 488 nm long pass filter.

Transient PL imaging was done using a home-build time-resolved single photon counting set-up including a 485 nm laser (PicoQuant LDH-D-C-485). The spatial mapping is performed by focusing the laser on the sample via a Nikon 60× water immersion objective (PlanAPO VC 60× A/1.2 WI) and the maps were collected with a piezo stage (PI-P-733.3CL). The luminescence was collected with a silicon-single photon avalanche detector (Micro Photon Devices, MPD-5CTD) and the set-up is controlled by a PicoQuant HydraHarp 400 event timer.

7. References:

(1) IPCC. *Climate Change 2021 The Physical Science Basis Summary for Policymakers*; 2021.

(2) DNV AS. *Energy Transition Outlook 2021. A Global and Regional Forecast to 2050.*; 2021.

(3) Lee, D. S.; Seo, S. W.; Park, M.-A.; Cheon, K. B.; Ji, S. G.; Park, I. J.; Kim, J. Y. Electrochemical Approach for Preparing Conformal Methylammonium Lead Iodide Layer. *Electrochem. commun.* **2019**, *103*, 120–126. https://doi.org/10.1016/j.elecom.2019.05.016.

(4) Lee, M. M.; Teuscher, J.; Miyasaka, T.; Murakami, T. N.; Snaith, H. J. Efficient Hybrid Solar Cells Based on Meso-Superstructured Organometal Halide Perovskites. *Science (80-.).* **2012**, *338* (6107), 643–647. https://doi.org/10.1126/science.1228604.

(5) Baranwal, A. K.; Masutani, H.; Sugita, H.; Kanda, H.; Kanaya, S.; Shibayama, N.; Sanehira, Y.; Ikegami, M.; Numata, Y.; Yamada, K.; Miyasaka, T.; Umeyama, T.; Imahori, H.; Ito, S. Lead-Free Perovskite Solar Cells Using Sb and Bi-Based A3B2X9 and A3BX6 Crystals with Normal and Inverse Cell Structures. *Nano Converg.* **2017**, *4* (1), 26. https://doi.org/10.1186/s40580-017-0120-3.

(6) Kim, H.-S.; Lee, C.-R.; Im, J.-H.; Lee, K.-B.; Moehl, T.; Marchioro, A.; Moon, S.-J.; Humphry-Baker, R.; Yum, J.-H.; Moser, J. E.; Grätzel, M.; Park, N.-G. Lead Iodide Perovskite Sensitized All-Solid-State Submicron Thin Film Mesoscopic Solar Cell with Efficiency Exceeding 9%. *Sci. Rep.* **2012**, *2* (1), 591. https://doi.org/10.1038/srep00591.

(7) Green, M.; Dunlop, E.; Hohl-Ebinger, J.; Yoshita, M.; Kopidakis, N.; Hao, X. Solar Cell Efficiency Tables (Version 57). *Prog. Photovoltaics Res. Appl.* **2021**, *29* (1), 3–15. https://doi.org/10.1002/pip.3371.

(8) Yi, Z.; Najib, A.; Ladi, H.; Shai, X.; Li, H.; Shen, Y.; Wang, M. Will Organic-Inorganic Hybrid Halide Lead Perovskites Be Eliminated from Optoelectronic Applications? **2019**. https://doi.org/10.1039/c8na00416a.

(9) Schmidt-Mende, L.; Dyakonov, V.; Olthof, S.; Ünlü, F.; Lê, K. M. T.; Mathur, S.; Karabanov, A. D.; Lupascu, D. C.; Herz, L. M.; Hinderhofer, A.; Schreiber, F.; Chernikov, A.; Egger, D. A.; Shargaieva, O.; Cocchi, C.; Unger, E.; Saliba, M.; Byranvand, M. M.; Kroll, M.; Nehm, F.; Leo, K.; Redinger, A.; Höcker, J.; Kirchartz, T.; Warby, J.; Gutierrez-Partida, E.; Neher, D.; Stolterfoht, M.; Würfel, U.; Unmüssig, M.; Herterich, J.; Baretzky, C.; Mohanraj, J.; Thelakkat, M.; Maheu, C.; Jaegermann, W.; Mayer, T.; Rieger, J.; Fauster, T.; Niesner, D.; Yang, F.; Albrecht, S.; Riedl, T.; Fakharuddin, A.; Vasilopoulou, M.; Vaynzof, Y.; Moia, D.; Maier, J.; Franckevičius, M.; Gulbinas, V.; Kerner, R. A.; Zhao, L.; Rand, B. P.; Glück, N.; Bein, T.; Matteocci, F.; Castriotta, L. A.; Di Carlo, A.; Scheffler, M.; Draxl, C. Roadmap on Organic-Inorganic Hybrid Perovskite Semiconductors and Devices. *APL Mater.* **2021**, *9* (10). https://doi.org/10.1063/5.0047616.

(10) Ossila. Perovskites and Perovskite Solar Cells: An Introduction https://www.ossila.com/pages/perovskites-and-perovskite-solar-cells-an-introduction

(accessed Jul 19, 2021).

(11) Stolterfoht, M.; Wolff, C. M.; Márquez, J. A.; Zhang, S.; Hages, C. J.; Rothhardt, D.; Albrecht, S.; Burn, P. L.; Meredith, P.; Unold, T.; Neher, D. Visualization and Suppression of Interfacial Recombination for High-Efficiency Large-Area Pin Perovskite Solar Cells. *Nat. Energy* **2018**, *3* (10), 847–854. https://doi.org/10.1038/s41560-018-0219-8.

(12) Chen, K.; Wu, P.; Yang, W.; Su, R.; Luo, D.; Yang, X.; Tu, Y.; Zhu, R.; Gong, Q. Low-Dimensional Perovskite Interlayer for Highly Efficient Lead-Free Formamidinium Tin Iodide Perovskite Solar Cells. *Nano Energy* **2018**, *49* (April), 411–418. https://doi.org/10.1016/j.nanoen.2018.05.006.

(13) Yang, W. S.; Park, B. W.; Jung, E. H.; Jeon, N. J.; Kim, Y. C.; Lee, D. U.; Shin, S. S.; Seo, J.; Kim, E. K.; Noh, J. H.; Seok, S. Il. Iodide Management in Formamidinium-Lead-Halide-Based Perovskite Layers for Efficient Solar Cells. *Science (80-.).* **2017**, *356* (6345), 1376–1379. https://doi.org/10.1126/science.aan2301.

(14) Tress, W. Perovskite Solar Cells on the Way to Their Radiative Efficiency Limit – Insights Into a Success Story of High Open-Circuit Voltage and Low Recombination. *Adv. Energy Mater.* **2017**, *7* (14). https://doi.org/10.1002/aenm.201602358.

(15) Stolterfoht, M.; Caprioglio, P.; Wolff, C. M.; Márquez, J. A.; Nordmann, J.; Zhang, S.; Rothhardt, D.; Hörmann, U.; Redinger, A.; Kegelmann, L.; Albrecht, S.; Kirchartz, T.; Saliba, M.; Unold, T.; Neher, D. The Perovskite/Transport Layer Interfaces Dominate Non-Radiative Recombination in Efficient Perovskite Solar Cells. **2018**, No. July, 1–23. https://doi.org/10.1039/c9ee02020a.

(16) Correa-Baena, J. P.; Tress, W.; Domanski, K.; Anaraki, E. H.; Turren-Cruz, S. H.; Roose, B.; Boix, P. P.; Grätzel, M.; Saliba, M.; Abate, A.; Hagfeldt, A. Identifying and Suppressing Interfacial Recombination to Achieve High Open-Circuit Voltage in Perovskite Solar Cells. *Energy Environ. Sci.* **2017**, *10* (5), 1207–1212. https://doi.org/10.1039/c7ee00421d.

(17) Tvingstedt, K.; Gil-Escrig, L.; Momblona, C.; Rieder, P.; Kiermasch, D.; Sessolo, M.; Baumann, A.; Bolink, H. J.; Dyakonov, V. Removing Leakage and Surface Recombination in Planar Perovskite Solar Cells. *ACS Energy Lett.* **2017**, *2* (2), 424–430. https://doi.org/10.1021/acsenergylett.6b00719.

(18) Wolff, C. M.; Zu, F.; Paulke, A.; Toro, L. P.; Koch, N.; Neher, D. Reduced Interface-Mediated Recombination for High Open-Circuit Voltages in CH3NH3PbI3 Solar Cells. *Adv. Mater.* **2017**, *29* (28), 1700159. https://doi.org/10.1002/adma.201700159.

(19) Wang, Q.; Dong, Q.; Li, T.; Gruverman, A.; Huang, J. Thin Insulating Tunneling Contacts for Efficient and Water-Resistant Perovskite Solar Cells. *Adv. Mater.* **2016**, *28* (31), 6734–6739. https://doi.org/10.1002/adma.201600969.

(20) Peng, J.; Khan, J. I.; Liu, W.; Ugur, E.; Duong, T.; Wu, Y.; Shen, H.; Wang, K.; Dang, H.; Aydin, E.; Yang, X.; Wan, Y.; Weber, K. J.; Catchpole, K. R.; Laquai, F.; De Wolf, S.; White, T. P. A Universal Double-Side Passivation for High Open-Circuit Voltage in Perovskite Solar Cells: Role of Carbonyl Groups in Poly(Methyl Methacrylate). *Adv. Energy Mater.* **2018**, *8* (30). https://doi.org/10.1002/aenm.201801208.

(21) Wong, J.; Yang, K. 2D Hybrid Halide Perovskites: Synthesis, Properties, and Applications. *Sol. RRL* **2021**, *5* (1), 53–56. https://doi.org/10.1002/solr.202000395.

(22) Koh, T. M.; Shanmugam, V.; Guo, X.; Lim, S. S.; Filonik, O.; Herzig, E. M.; Müller-Buschbaum, P.; Swamy, V.; Chien, S. T.; Mhaisalkar, S. G.; Mathews, N. Enhancing Moisture Tolerance in Efficient Hybrid 3D/2D Perovskite Photovoltaics. *J. Mater. Chem. A* **2018**, *6* (5), 2122–2128. https://doi.org/10.1039/c7ta09657g.

(23) Gao, P.; Bin Mohd Yusoff, A. R.; Nazeeruddin, M. K. Dimensionality Engineering of Hybrid Halide Perovskite Light Absorbers. *Nat. Commun.* **2018**, *9* (1), 5028. https://doi.org/10.1038/s41467-018-07382-9.

(24) Grancini, G.; Roldán-Carmona, C.; Zimmermann, I.; Mosconi, E.; Lee, X.; Martineau, D.; Narbey, S.; Oswald, F.; De Angelis, F.; Graetzel, M.; Nazeeruddin, M. K. One-Year Stable Perovskite Solar Cells by 2D/3D Interface Engineering. *Nat. Commun.* **2017**, *8* (1), 15684. https://doi.org/10.1038/ncomms15684.

(25) Du, K. Z.; Tu, Q.; Zhang, X.; Han, Q.; Liu, J.; Zauscher, S.; Mitzi, D. B. Two-Dimensional Lead(II) Halide-Based Hybrid Perovskites Templated by Acene Alkylamines: Crystal Structures, Optical Properties, and Piezoelectricity. *Inorg. Chem.* **2017**, *56* (15), 9291–9302. https://doi.org/10.1021/acs.inorgchem.7b01094.

(26) Li, X.; Hoffman, J. M.; Kanatzidis, M. G. The 2D Halide Perovskite Rulebook: How the Spacer Influences Everything from the Structure to Optoelectronic Device Efficiency. *Chem. Rev.* **2021**, *121* (4), 2230–2291. https://doi.org/10.1021/acs.chemrev.0c01006.

(27) Krishna, A.; Gottis, S.; Nazeeruddin, M. K.; Sauvage, F. Mixed Dimensional 2D/3D Hybrid Perovskite Absorbers: The Future of Perovskite Solar Cells? *Adv. Funct. Mater.* **2019**, *29* (8). https://doi.org/10.1002/adfm.201806482.

(28) Niu, T.; Lu, J.; Jia, X.; Xu, Z.; Tang, M. C.; Barrit, D.; Yuan, N.; Ding, J.; Zhang, X.; Fan, Y.; Luo, T.; Zhang, Y.; Smilgies, D. M.; Liu, Z.; Amassian, A.; Jin, S.; Zhao, K.; Liu, S. Interfacial Engineering at the 2D/3D Heterojunction for High-Performance Perovskite Solar Cells. *Nano Lett.* **2019**, *19* (10), 7181–7190. https://doi.org/10.1021/acs.nanolett.9b02781.

(29) Wang, Z.; Lin, Q.; Chmiel, F. P.; Sakai, N.; Herz, L. M.; Snaith, H. J. Efficient Ambient-Air-Stable Solar Cells with 2D-3D Heterostructured Butylammonium-Caesium-Formamidinium Lead Halide Perovskites. *Nat. Energy* **2017**, *2* (9), 1–10. https://doi.org/10.1038/nenergy.2017.135.

(30) Li, P.; Zhang, Y.; Liang, C.; Xing, G.; Liu, X.; Li, F.; Liu, X.; Hu, X.; Shao, G.; Song, Y. Phase Pure 2D Perovskite for High-Performance 2D–3D Heterostructured Perovskite Solar Cells. *Adv. Mater.* **2018**, *30* (52), 1805323. https://doi.org/10.1002/adma.201805323.

(31) Ma, C.; Leng, C.; Ji, Y.; Wei, X.; Sun, K.; Tang, L.; Yang, J.; Luo, W.; Li, C.; Deng, Y.; Feng, S.; Shen, J.; Lu, S.; Du, C.; Shi, H. 2D/3D Perovskite Hybrids as Moisture-Tolerant and Efficient Light Absorbers for Solar Cells. *Nanoscale* **2016**, *8* (43), 18309–18314. https://doi.org/10.1039/c6nr04741f.

(32) Liu, Y.; Akin, S.; Pan, L.; Uchida, R.; Arora, N.; Milić, J. V.; Hinderhofer, A.; Schreiber, F.; Uhl, A. R.; Zakeeruddin, S. M.; Hagfeldt, A.; Ibrahim Dar, M.; Grätzel, M. Ultrahydrophobic 3D/2D Fluoroarene Bilayer-Based Water-Resistant Perovskite Solar Cells with Efficiencies Exceeding 22%. *Sci. Adv.* **2019**, *5* (6). https://doi.org/10.1126/sciadv.aaw2543.

(33) Yoo, J. J.; Wieghold, S.; Sponseller, M. C.; Chua, M. R.; Bertram, S. N.; Hartono, N. T. P.; Tresback, J. S.; Hansen, E. C.; Correa-Baena, J. P.; Bulović, V.; Buonassisi, T.; Shin, S. S.; Bawendi, M. G. An Interface Stabilized Perovskite Solar Cell with High Stabilized Efficiency and Low Voltage Loss. *Energy Environ. Sci.* **2019**, *12* (7), 2192–2199. https://doi.org/10.1039/c9ee00751b.

(34) Jung, E. H.; Jeon, N. J.; Park, E. Y.; Moon, C. S.; Shin, T. J.; Yang, T. Y.; Noh, J. H.; Seo, J. Efficient, Stable and Scalable Perovskite Solar Cells Using Poly(3-Hexylthiophene). *Nature* **2019**, *567* (7749), 511–515. https://doi.org/10.1038/s41586-019-1036-3.

(35) Liu, J.; Leng, J.; Wu, K.; Zhang, J.; Jin, S. Observation of Internal Photoinduced Electron and Hole Separation in Hybrid Two-Dimentional Perovskite Films. *J. Am. Chem. Soc.* **2017**, *139* (4), 1432–1435. https://doi.org/10.1021/jacs.6b12581.

(36) Lin, D.; Zhang, T.; Wang, J.; Long, M.; Xie, F.; Chen, J.; Wu, B.; Shi, T.; Yan, K.; Xie, W.; Liu, P.; Xu, J. Stable and Scalable 3D-2D Planar Heterojunction Perovskite Solar Cells via Vapor Deposition. *Nano Energy* **2019**, *59* (December 2018), 619–625. https://doi.org/10.1016/j.nanoen.2019.03.014.

(37) La-Placa, M.-G.; Gil-Escrig, L.; Guo, D.; Palazon, F.; Savenije, T. J.; Sessolo, M.; Bolink, H. J. Vacuum-Deposited 2D/3D Perovskite Heterojunctions. *ACS Energy Lett.* **2019**, *4* (12), 2893–2901. https://doi.org/10.1021/acsenergylett.9b02224.

(38) La-Placa, M. G.; Guo, D.; Gil-Escrig, L.; Palazon, F.; Sessolo, M.; Bolink, H. J. Dual-Source Vacuum Deposition of Pure and Mixed Halide 2D Perovskites: Thin Film Characterization and Processing Guidelines. *J. Mater. Chem. C* **2020**, *8* (6), 1902–1908. https://doi.org/10.1039/c9tc06662d.

(39) Jang, Y. W.; Lee, S.; Yeom, K. M.; Jeong, K.; Choi, K.; Choi, M.; Noh, J. H. Intact 2D/3D Halide Junction Perovskite Solar Cells via Solid-Phase in-Plane Growth. *Nat. Energy* **2021**, *6* (1), 63–71. https://doi.org/10.1038/s41560-020-00749-7.

(40) Alsari, M.; Bikondoa, O.; Bishop, J.; Abdi-Jalebi, M.; Ozer, L. Y.; Hampton, M.; Thompson, P.; Hörantner, M. T.; Mahesh, S.; Greenland, C.; Macdonald, J. E.; Palmisano, G.; Snaith, H. J.; Lidzey, D. G.; Stranks, S. D.; Friend, R. H.; Lilliu, S. In Situ Simultaneous Photovoltaic and Structural Evolution of Perovskite Solar Cells during Film Formation. *Energy Environ. Sci.* **2018**, *11* (2), 383–393. https://doi.org/10.1039/c7ee03013d.

(41) Tainter, G. D.; Hörantner, M. T.; Pazos-Outón, L. M.; Lamboll, R. D.; Āboliņš, H.; Leijtens, T.; Mahesh, S.; Friend, R. H.; Snaith, H. J.; Joyce, H. J.; Deschler, F. Long-Range Charge Extraction in Back-Contact Perovskite Architectures via Suppressed Recombination. *Joule* **2019**, *3* (5), 1301–1313. https://doi.org/10.1016/j.joule.2019.03.010.

(42) La-Placa, M. G.; Gil-Escrig, L.; Guo, D.; Palazon, F.; Savenije, T. J.; Sessolo, M.; Bolink, H. J. Vacuum-Deposited 2D/3D Perovskite Heterojunctions. *ACS Energy Lett.* **2019**, *4* (12), 2893–2901. https://doi.org/10.1021/acsenergylett.9b02224.

(43) Li, C.; Iqbal, M.; Lin, J.; Luo, X.; Jiang, B.; Malgras, V.; Wu, K. C. W.; Kim, J.; Yamauchi, Y. Electrochemical Deposition: An Advanced Approach for Templated Synthesis of Nanoporous Metal Architectures. *Acc. Chem. Res.* **2018**, *51* (8), 1764–1773. https://doi.org/10.1021/acs.accounts.8b00119.

(44) Cui, X.-P.; Jiang, K.-J.; Huang, J.-H.; Zhou, X.-Q.; Su, M.-J.; Li, S.-G.; Zhang, Q.-Q.; Yang, L.-M.; Song, Y.-L. Electrodeposition of PbO and Its in Situ Conversion to CH 3 NH 3 PbI 3 for Mesoscopic Perovskite Solar Cells. *Chem. Commun.* **2015**, *51* (8), 1457–1460. https://doi.org/10.1039/C4CC08269A.

(45) Popov, G.; Mattinen, M.; Kemell, M. L.; Ritala, M.; Leskelä, M. Scalable Route to the Fabrication of CH 3 NH 3 PbI 3 Perovskite Thin Films by Electrodeposition and Vapor Conversion. *ACS Omega* **2016**, *1* (6), 1296–1306. https://doi.org/10.1021/acsomega.6b00351.

(46) Liu, D.; Liu, K.; Liu, Y.; Bai, J.; Dai, M.; Liu, F.; Lu, G. Low-Voltage Room-Temperature Electrochemical Deposition of Perovskite Films for Solar Cell Devices. *Sol. Energy* **2020**, *212* (October), 275–281. https://doi.org/10.1016/j.solener.2020.11.010.

(47) Chen, H.; Wei, Z.; Zheng, X.; Yang, S. A Scalable Electrodeposition Route to the Low-Cost, Versatile and Controllable Fabrication of Perovskite Solar Cells. *Nano Energy* **2015**, *15*, 216–226. https://doi.org/10.1016/j.nanoen.2015.04.025.

(48) Zanca, C.; Piazza, V.; Agnello, S.; Patella, B.; Ganci, F.; Aiello, G.; Piazza, S.; Sunseri, C.; Inguanta, R. Controlled Solution-Based Fabrication of Perovskite Thin Films Directly on Conductive Substrate. *Thin Solid Films* **2021**, *733* (September 2021). https://doi.org/10.1016/j.tsf.2021.138806.

(49) Lee, D. S.; Seo, S. W.; Park, M. A.; Cheon, K. B.; Ji, S. G.; Park, I. J.; Kim, J. Y. Electrochemical Approach for Preparing Conformal Methylammonium Lead Iodide Layer. *Electrochem. commun.* **2019**, *103* (May), 120–126. https://doi.org/10.1016/j.elecom.2019.05.016.

(50) Koza, J. A.; Hill, J. C.; Demster, A. C.; Switzer, J. A. Epitaxial Electrodeposition of Methylammonium Lead Iodide Perovskites. *Chem. Mater.* **2016**, *28* (1), 399–405. https://doi.org/10.1021/acs.chemmater.5b04524.

(51) Lekina, Y.; Shen, Z. X. Excitonic States and Structural Stability in Two-Dimensional Hybrid Organic-Inorganic Perovskites. *J. Sci. Adv. Mater. Devices* **2019**, *4* (2), 189–200. https://doi.org/10.1016/j.jsamd.2019.03.005.

(52) Cao, D. H.; Stoumpos, C. C.; Farha, O. K.; Hupp, J. T.; Kanatzidis, M. G. 2D Homologous Perovskites as Light-Absorbing Materials for Solar Cell Applications. *J. Am. Chem. Soc.* **2015**, *137* (24), 7843–7850. https://doi.org/10.1021/JACS.5B03796/SUPPL_FILE/JA5B03796_SI_001.PDF.

(53) McMeekin, D. P.; Sadoughi, G.; Rehman, W.; Eperon, G. E.; Saliba, M.; Hörantner, M. T.; Haghighirad, A.; Sakai, N.; Korte, L.; Rech, B.; Johnston, M. B.; Herz, L. M.; Snaith, H. J. A Mixed-Cation Lead Mixed-Halide Perovskite Absorber for Tandem Solar Cells. *Science (80-.).* **2016**, *351* (6269), 151–155. https://doi.org/10.1126/science.aad5845.

(54) Decker, W.; Belan, R.; Heydemann, V.; Armstrong, S.; Fisher, T. Novel Low Pressure Sputtering Source and Improved Vacuum Deposition of Small Patterned Features Using Precision Shadow Masks. *Web Coat. Handl. Conf. 2016, WCHC 2016* **2016**, *1* (May), 556–571. https://doi.org/10.14332/svc16.proc.0036.

(55) Lee, S.; Kruse, J. Biopotential Electrode Sensors in ECG/EEG/EMG Systems. *Motorcontrol.Analog.Com* **2008**, 1–2.

(56) Valenti, M.; Bleiji, Y.; Portals, J. B.; Muscarella, L. A.; Aarts, M.; Peiro, F.; Estrade, S.; Alarcón-Lladó, E. Grain Size Control of Crystalline III–V Semiconductors at Ambient Conditions Using Electrochemically Mediated Growth. *J. Mater. Chem. A* **2020**, *8* (5), 2752–2759. https://doi.org/10.1039/C9TA07410D.

(57) Li, X.; Pletcher, D.; Walsh, F. C. Electrodeposited Lead Dioxide Coatings. *Chem. Soc. Rev.* **2011**, *40* (7), 3879–3894. https://doi.org/10.1039/c0cs00213e.

(58) Persson, K. Materials Data on PbO2 (SG:136) by Materials Project. 2014. https://doi.org/10.17188/1195886.

(59) Velichenko, A. B.; Baranova, E. A.; Girenko, D. V.; Amadelli, R.; Kovalev, S. V.; Danilov, F. I. Mechanism of Electrodeposition of Lead Dioxide from Nitrate Solutions. *Russ. J. Electrochem.* **2003**, *39* (6), 615–621. https://doi.org/10.1023/A:1024101210790.

(60) Mahalingam, T.; Velumani, S.; Raja, M.; Thanikaikarasan, S.; Chu, J. P.; Wang, S. F.; Kim, Y. D. Electrosynthesis and Characterization of Lead Oxide Thin Films. *Mater. Charact.* **2007**, *58* (8-9 SPEC. ISS.), 817–822. https://doi.org/10.1016/J.MATCHAR.2006.11.021.

(61) Franklin, R. K.; Martin, S. M.; Strong, T. D.; Brown, R. B. *Chemical and Biological Systems: Chemical Sensing Systems for Liquids*; Elsevier Ltd., 2016. https://doi.org/10.1016/b978-0-12-803581-8.00549-x.

(62) Sirés, I.; Low, C. T. J.; Ponce-de-León, C.; Walsh, F. C. The Characterisation of PbO2-Coated Electrodes Prepared from Aqueous Methanesulfonic Acid under Controlled Deposition Conditions. *Electrochim. Acta* **2010**, *55* (6), 2163–2172. https://doi.org/10.1016/j.electacta.2009.11.051.

(63) Munichandraiah, N. Physicochemical Properties of Electrodeposited β-Lead Dioxide: Effect of Deposition Current Density. *J. Appl. Electrochem.* **1992**, *22* (9), 825–829. https://doi.org/10.1007/BF01023725.

(64) Saterlay, A. J.; Wilkins, S. J.; Holt, K. B.; Foord, J. S.; Compton, R. G.; Marken, F. Lead Dioxide Deposition and Electrocatalysis at Highly Boron-Doped Diamond Electrodes in the Presence of Ultrasound. *J. Electrochem. Soc.* **2001**, *148* (2), E66. https://doi.org/10.1149/1.1339874.

(65) Devilliers, D.; Dinh Thi, M. T.; Mahé, E.; Dauriac, V.; Lequeux, N. Electroanalytical Investigations on Electrodeposited Lead Dioxide. *J. Electroanal. Chem.* **2004**, *573* (2), 227–239. https://doi.org/10.1016/j.jelechem.2004.07.008.

(66) Gnanasekaran, K. S. A.; Narasimham, K. C.; Udupa, H. V. K. Stress Measurements in Electrodeposited Lead Dioxide. *Electrochim. Acta* **1970**, *15* (10), 1615–1622. https://doi.org/10.1016/0013-4686(70)80083-4.

(67) Thanos, J. C. G.; Wabner, D. W. Specific Orientation of Electrochemically Deposited PbO2 Crystals. *J. Electroanal. Chem.* **1985**, *182* (1), 25–36. https://doi.org/10.1016/0368-1874(85)85437-X.

(68) Shen, P. K.; Wei, X. L. Morphologic Study of Electrochemically Formed Lead Dioxide. *Electrochim. Acta* **2003**, *48* (12), 1743–1747. https://doi.org/10.1016/S0013-4686(03)00149-X.

(69) Low, C. T. J.; Pletcher, D.; Walsh, F. C. The Electrodeposition of Highly Reflective

Lead Dioxide Coatings. *Electrochem. commun.* **2009**, *11* (6), 1301–1304. https://doi.org/10.1016/j.elecom.2009.04.032.

(70) Liu, Y.; Liu, H. Comparative Studies on the Electrocatalytic Properties of Modified PbO2 Anodes. *Electrochim. Acta* **2008**, *53* (16), 5077–5083. https://doi.org/10.1016/j.electacta.2008.02.103.

(71) Moser, T.; Artuk, K.; Jiang, Y.; Feurer, T.; Gilshtein, E.; Tiwari, A. N.; Fu, F. Revealing the Perovskite Formation Kinetics during Chemical Vapour Deposition. *J. Mater. Chem. A* **2020**, *8* (42), 21973–21982. https://doi.org/10.1039/d0ta04501b.

(72) Kaur, N.; Comini, E.; Poli, N.; Zappa, D.; Sberveglieri, G. Nickel Oxide Nanowires Growth by VLS Technique for Gas Sensing Application. *Procedia Eng.* **2015**, *120* (September), 760–763. https://doi.org/10.1016/j.proeng.2015.08.805.

(73) Sun, L.; Chen, J. Y.; Jiang, W.; Lynch, V. Crystalline Characteristics of Cellulose Fiber and Film Regenerated from Ionic Liquid Solution. *Carbohydr. Polym.* **2015**, *118*, 150–155. https://doi.org/10.1016/j.carbpol.2014.11.008.

(74) Huang, J.; Jiang, K.; Cui, X.; Zhang, Q.; Gao, M.; Su, M.; Yang, L.; Song, Y. Direct Conversion of CH3NH3PbI3 from Electrodeposited PbO for Highly Efficient Planar Perovskite Solar Cells. *Sci. Rep.* **2015**, *5* (1), 15889. https://doi.org/10.1038/srep15889.

(75) Heydari, Z.; Abdy, H.; Madani, M.; Ghaziani, M. P.; Kolahdouz, M.; Asl-Soleimani, E. A Novel Approach for Preparation of CH3NH3PbBr3 via Direct Transformation of Electrodeposited PbO2 for Photodetector Application. *J. Mater. Sci. Mater. Electron.* **2020**, *31* (1), 154–160. https://doi.org/10.1007/s10854-019-02438-y.

(76) Banik, S. J.; Akolkar, R. Suppressing Dendritic Growth during Alkaline Zinc Electrodeposition Using Polyethylenimine Additive. *Electrochim. Acta* **2015**, *179*, 475–481. https://doi.org/10.1016/J.ELECTACTA.2014.12.100.

(77) Abdy, H.; Heydari, Z.; Aletayeb, A.; Kolahdouz, M.; Asl-Soleimani, E. Electrodeposition, Solvent Engineering, and Two-Step Solution Deposition of the Perovskite Films: Morphological and Structural Study. *J. Mater. Sci. Mater. Electron.* **2021**, *32* (10), 12991–12999. https://doi.org/10.1007/s10854-020-03609-y.

(78) Heydari, Z.; Abdy, H.; Ghaziani, M. P.; Kolahdouz, M.; Asl-Soleimani, E.; Masnadi-Shirazi, M. Effect of CH3NH3I/CH3NH3Br Precursors on the Structural and Surface Morphology Properties of the Electrodeposited Methylammonium Lead–Mixed Halide Perovskite Films. *J. Solid State Electrochem.* **2021**, *25* (2), 583–590. https://doi.org/10.1007/s10008-020-04830-9.

(79) Yao, Z.; Wang, W.; Shen, H.; Zhang, Y.; Luo, Q.; Yin, X.; Dai, X.; Li, J.; Lin, H. CH 3 NH 3 PbI 3 Grain Growth and Interfacial Properties in Meso-Structured Perovskite Solar Cells Fabricated by Two-Step Deposition. *Sci. Technol. Adv. Mater.* **2017**, *18* (1), 253–262. https://doi.org/10.1080/14686996.2017.1298974.

(80) Zhang, J.; Zhu, X.; Wang, M.; Hu, B. Establishing Charge-Transfer Excitons in 2D Perovskite Heterostructures. *Nat. Commun.* **2020**, *11* (1), 2618. https://doi.org/10.1038/s41467-020-16415-1.

(81) Swartwout, R.; Hoerantner, M. T.; Bulović, V. Scalable Deposition Methods for Large-Area Production of Perovskite Thin Films. *Energy Environ. Mater.* **2019**, *2* (2), 119–145. https://doi.org/10.1002/eem2.12043.

(82) Perez, R. Controlled Deposition of Fullerenes. **2018**, No. December. https://doi.org/10.13140/RG.2.2.31031.78247.

(83) Ham, A.; Kim, T. S.; Kang, M.; Cho, H.; Kang, K. Strategies for Chemical Vapor Deposition of Two-Dimensional Organic-Inorganic Halide Perovskites. *iScience* **2021**, *24* (12), 103486. https://doi.org/10.1016/j.isci.2021.103486.

(84) Hu, Y.; Schlipf, J.; Wussler, M.; Petrus, M. L.; Jaegermann, W.; Bein, T.; Müller-Buschbaum, P.; Docampo, P. Hybrid Perovskite/Perovskite Heterojunction Solar Cells. *ACS Nano* **2016**, *10* (6), 5999–6007. https://doi.org/10.1021/acsnano.6b01535.

(85) Proppe, A. H.; Johnston, A.; Teale, S.; Mahata, A.; Quintero-Bermudez, R.; Jung, E. H.; Grater, L.; Cui, T.; Filleter, T.; Kim, C. Y.; Kelley, S. O.; De Angelis, F.; Sargent, E. H. Multication Perovskite 2D/3D Interfaces Form via Progressive Dimensional Reduction. *Nat. Commun.* **2021**, *12* (1), 1–9. https://doi.org/10.1038/s41467-021-23616-9.

(86) Chiang, Y. H.; Anaya, M.; Stranks, S. D. Multisource Vacuum Deposition of Methylammonium-Free Perovskite Solar Cells. *ACS Energy Lett.* **2020**, *5* (8), 2498–2504. https://doi.org/10.1021/acsenergylett.0c00839.

(87) Song, Y.; Zhang, C.; Liu, W.; Li, X.; Long, H.; Wang, K.; Wang, B.; Lu, P. High-Efficiency Energy Transfer in Perovskite Heterostructures. *Opt. Express* **2018**, *26* (14), 18448. https://doi.org/10.1364/oe.26.018448.

(88) Lin, Y.; Fang, Y.; Zhao, J.; Shao, Y.; Stuard, S. J.; Nahid, M. M.; Ade, H.; Wang, Q.; Shield, J. E.; Zhou, N.; Moran, A. M.; Huang, J. Unveiling the Operation Mechanism of Layered Perovskite Solar Cells. *Nat. Commun.* **2019**, *10* (1). https://doi.org/10.1038/S41467-019-08958-9.